Coastal Engineering 178 (2022) 104204

Contents lists available at ScienceDirect

Coastal Engineering

journal homepage: www.elsevier.com/locate/coastaleng

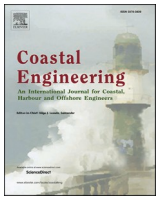

Numerical modeling of hydrodynamics on an elevated residential structure from varied wave and surge conditions using OpenFOAM

Dayeon Lee [a], Hyoungsu Park [b], Taemin Ha [c], Sungwon Shin [d,*], Daniel T. Cox [e]

[a] Department of Marine and Convergent Technology, Hanyang University ERICA, Ansan, Republic of Korea
[b] Department of Civil and Environmental Engineering, College of Engineering, University of Hawaii at Mānoa, USA
[c] Department of Civil Engineering, Kangwon National University, Samcheok, Republic of Korea
[d] Department of Marine Science and Convergence Engineering, Hanyang University ERICA, Ansan, Republic of Korea
[e] School of Civil and Construction Engineering, Oregon State University, Corvallis, OR, 97331-2302, USA

ARTICLE INFO

Keywords:
Hurricane
OpenFOAM
Elevated structures
Force
Air gap

ABSTRACT

A Computational Fluid Dynamic (CFD) model study of wave and structure interactions on an elevated residential building under various air gap and surge/wave conditions was performed using the olaFlow, an open-source program using the OpenFOAM (Open-source Fields Operation And Manipulation) platform. The numerical model results, including free surface elevation, wave velocity, and vertical pressures on the underside of the elevated structure, showed a good agreement with the measured time-series data from the 1:6 scale hydraulic experiment (Duncan et al., 2021). The numerical simulations were used to extend the physical model tests by computing the vertical distribution of the pressure and resulting wave-induced horizontal forces/pressures, which were not measured in the physical model studies. The simulated results indicate that the pattern of pressure distributions at the frontal face of the elevated structure was controlled by water depth and wave-breaking types (nonbreaking, breaking, and broken waves). The wave induced-vertical force on the elevated structure strongly depends on wave height and the air gap, which is a net elevation from the still water level to the bottom of the structure, but the horizontal force shows complicated patterns due to the varied surge levels (flow depth), wave heights and air gaps. The new dimensionless parameter, α'/h, comprised of the air gap, incident wave height, and flow depth, is introduced and utilized to predict the horizontal forces on the elevated structure.

1. Introduction

Low-lying coastal regions are most vulnerable to extreme coastal flooding events such as storm surges and waves generated by hurricanes and typhoons. With the global sea-level rise (SLR) threats, climate change may lead to stronger tropical storms by making sea-level temperatures hotter (e.g., Różyński et al., 2009; IPCC, 2021). According to Mendelsohn et al. (2012), the annual tropical cyclone damage was estimated to be $26 billion worldwide. In the United States, hurricanes have been listed in seven of the top 10 disasters that have caused the most damage since 1980 (Lackey, 2011), and Desai et al. (2019) emphasized the fact that more than 7.3 million residential homes on the Gulf and Atlantic coasts have the risk of storm surge damage. Particularly, the series of hurricanes, such as Hurricanes Katrina, Ike, Sandy, and Harvey, have caused widespread damage to residential buildings and infrastructure and devastated coastal communities on the US coasts (Kennedy et al., 2011; Pistrika and Jonkman, 2010; Xian et al., 2015). Significantly, the elevated residential structure is widespread as an adaptation measure in coastal communities along the Gulf and East Coast of the U.S. (e.g., Small et al., 2016). Still, the elevated structures are vulnerable to damage caused by surges and waves, as evidenced by their performance in past hurricanes (e.g., Tomiczek et al., 2013). Therefore, a better understanding of the loading mechanism on the elevated structure is essential to predict and quantify damages and losses from future extreme wave climates.

Several studies have quantified the loading on elevated coastal structures like coastal bridges, jetties, or offshore platforms. Kaplan et al. (1995) developed a mathematical model based on momentum flux to

* Corresponding author.
E-mail addresses: dyl12638@gmail.com (D. Lee), hpark9@hawaii.edu (H. Park), tmha@kangwon.ac.kr (T. Ha), sungwshin@hanyang.ac.kr (S. Shin), dan.cox@oregonstate.edu (D.T. Cox).

https://doi.org/10.1016/j.coastaleng.2022.104204
Received 24 March 2022; Received in revised form 18 August 2022; Accepted 28 August 2022
Available online 2 September 2022

predict the time history of impact loading on offshore platforms and the wave impact force from large incident waves. The impulsive breaking wave forces at the deck were evaluated through experimental studies (Bea et al., 1999). Cuomo et al. (2007) performed a 1:25 scale experiment of wave forces and deduced new dimensionless predictive solutions. The new solution utilized a linear correlation of the effective measure of water that inundates the deck and wave height to horizontal force on jetties. Cuomo et al. (2009) also conducted a 1:10 scaled physical model test of wave forces on a highway bridge and presented the new dimensionless predictive formulas by comparing physical model results. More recently, a 1:5 scale physical experiment was performed by Bradner et al. (2011) using a concrete bridge deck with different wave heights and periods in varying water depths. They observed that the buildings with the lowest horizontal structural members (LHM) above a certain height were more likely to survive.

More recently, there have been several studies on the damage to elevated structures built along the coast, such as residential structures, which are typically not designed to withstand wave loads. Kennedy et al. (2011) conducted field surveys after Hurricane Ike in 2008 and found that the elevation of the building from the ground is the most critical factor for the building's survival in the storm condition. Tomiczek et al. (2013) used the post-hurricane Ike survey of damage to wood-frame residential houses to improve fragility and damage models, which conclude that house freeboard, wave height, and water velocity are the most critical factors of the probability of failure. Xian et al. (2015) and Hatzikyriakou et al. (2016) observed that building performance in the community is significantly affected by the distance of the buildings from the coast, elevation from the ground, age of buildings, and flow shielding and channeling effects due to the presence of neighboring buildings.

Besides field works, there have been some efforts to understand the wave forces on residential structures through physical modeling in hydraulic laboratories. Wilson (2008) conducted physical model experiments using a 1:6 scale wood-frame residential structure to evaluate the impacts of storm surged wave loadings on the structure. The same physical model was utilized for the tsunami-like solitary wave loadings (van de Lindt et al., 2009). Park et al. (2017) performed a 1/10 scale laboratory experiment to characterize the wave-induced horizontal and vertical forces acting on the elevated structure using an idealized solid box-shaped specimen under varied air gaps. The effects of the air gap were studied by directly raising and lowing the specimen keeping the same surge and wave conditions. Recently, 1:6 scale physical model experiments were performed to measure the structural responses and damage states on the non-rigid elevated wood structure and slab on grade structure under varied storm surge and wave conditions (Duncan et al., 2021). The experiment successfully generated a large-scale wooden elevated structure with structural components including windows, gates, inner columns, and walls. The results of structural response and the hydrodynamic pressure on the bottom of the elevated specimen revealed that the pressure distribution and the resulting vertical forces were positively correlated to water depth, wave height, and air gap. The scaled physical experiment results were utilized to predict the horizontal and vertical loading and distribution of pressures on the elevated structure, Wiebe et al. (2014) first suggested an analytical solution to predict the horizontal forces on an elevated structure by modifying Goda's pressure equation (Goda, 1974, 2010) and Tomiczek et al. (2019) validated and extended the same approach of Wiebe et al. (2014) with the measured horizontal and vertical pressures data from Park et al. (2017).

In addition, high-resolution Computational Fluid Dynamics (CFD) approaches have been used to estimate wave-induced pressures and forces on the elevated structure under various hydrodynamics and structural conditions. Particularly for the elevated structures, the most typical studies were performed with a bridge deck under the varied profile of bridge deck, water depth, and wave conditions (Hayatdavoodi et al., 2014; Seiffert et al., 2015; Wu, 2016; Chen et al., 2016; Huang et al., 2018; Do et al., 2020). However, the bathymetry and prevailing wave conditions on a bridge deck during storms and the profile of a superstructure are significantly different from the elevated residential structure located onshore. Therefore, the major findings from experimental and numerical studies of bridge decks can neither properly understand nor predict the forces to evaluate the performance of the elevated residential structure during storm conditions.

Park et al. (2018) performed a quantitative CFD model comparison between OpenFOAM and ANSYS-fluent through 1/10 scale physical model data from Park et al. (2017). They investigated the wave-induced pressures and forces acting on the simple box-shape and elevated structure under varied air gaps and wave conditions. The studies highlighted the application of CFD models to evaluate the pressure and force on the elevated structures. They concluded that the dominant vertical force occurs at the zero-air gap at the non-breaking wave, while the horizontal force was dominant from the breaking types and air gap conditions. More recently, Do et al. (2020) numerically modeled the storm surge and wave loadings at complex building components, including windows, doors, walls, and floor systems for elevated structures. However, the actual physical experiment data did not fully validate the numerical model.

In this study, we utilize the experimental setup and data from wave conditions of the 1/6 scaled elevated structure (Duncan et al., 2021), which have similar characteristics of structural details (two stores, windows, gates, inside walls) to full-scale structures. Since Duncan et al. (2021) only measured vertical loadings from the series of pressure sensors at the bottom, our numerical model studies focus on quantifying the missed horizontal forces and pressure distributions at the front. We first validate our numerical model setup by comparing it with the structure's measured time-series surface elevation, velocity, and vertical pressure data. Then, we evaluate detailed characteristics of the elevated structure's horizontal pressure distributions and forces under varied surge and wave conditions. Therefore, there are three main objectives in this study: (1) validate a numerical model (olaFlow) set up for the physical experiment at 1:6 scaled an on elevated wooden structure (Duncan et al., 2021) for a series of tested waves and surge conditions; (2) investigate the spatial pressure distribution and total horizontal forces, acting on the elevated residential structure under varying wave heights, surge levels, and breaking types (non-breaking, impulsive breaking, broken); and (3) find the correlations between wave height and surge levels at the specimen to the wave induced-pressure distributions on the specimen, and characterize the wave-induced loading on the elevated residential structure.

This paper is outlined as follows. Section 2 gives the general information about the experiment setup, including the detailed instrumentation and test conditions. Section 3 introduces the overview of the numerical model and details of the model setup. Section 4 compares the numerical model results to the observed physical model results. Section 5 presents the simulated results to evaluate the horizontal pressure distribution and vertical and horizontal forces acting on the specimen. Finally, Section 6 concludes the paper with a summary of the results.

2. Experimental setup

2.1. Experimental design

The numerical model study utilizes the 1:6 scaled physical experiments performed at the Directional Tsunami Wave Basin at the O. H. Hinsdale Wave Research Laboratory (HWRL) at Oregon State University. The experimental data have been archived on DesignSafe.org and are available to the public (Cox et al., 2021; https://doi.org/10.17603/ds2-8evm-1y60). An overview of the data is described here and in more detail in Duncan et al. (2021). The plan and profile view of the physical experiment setup, including locations of the instrument in the Directional Tsunami Wave Basin, are shown in Fig. 1. The dimensions of the basin were 48.8 m long (x-direction), 26.5 m wide (y-direction), and 2.1

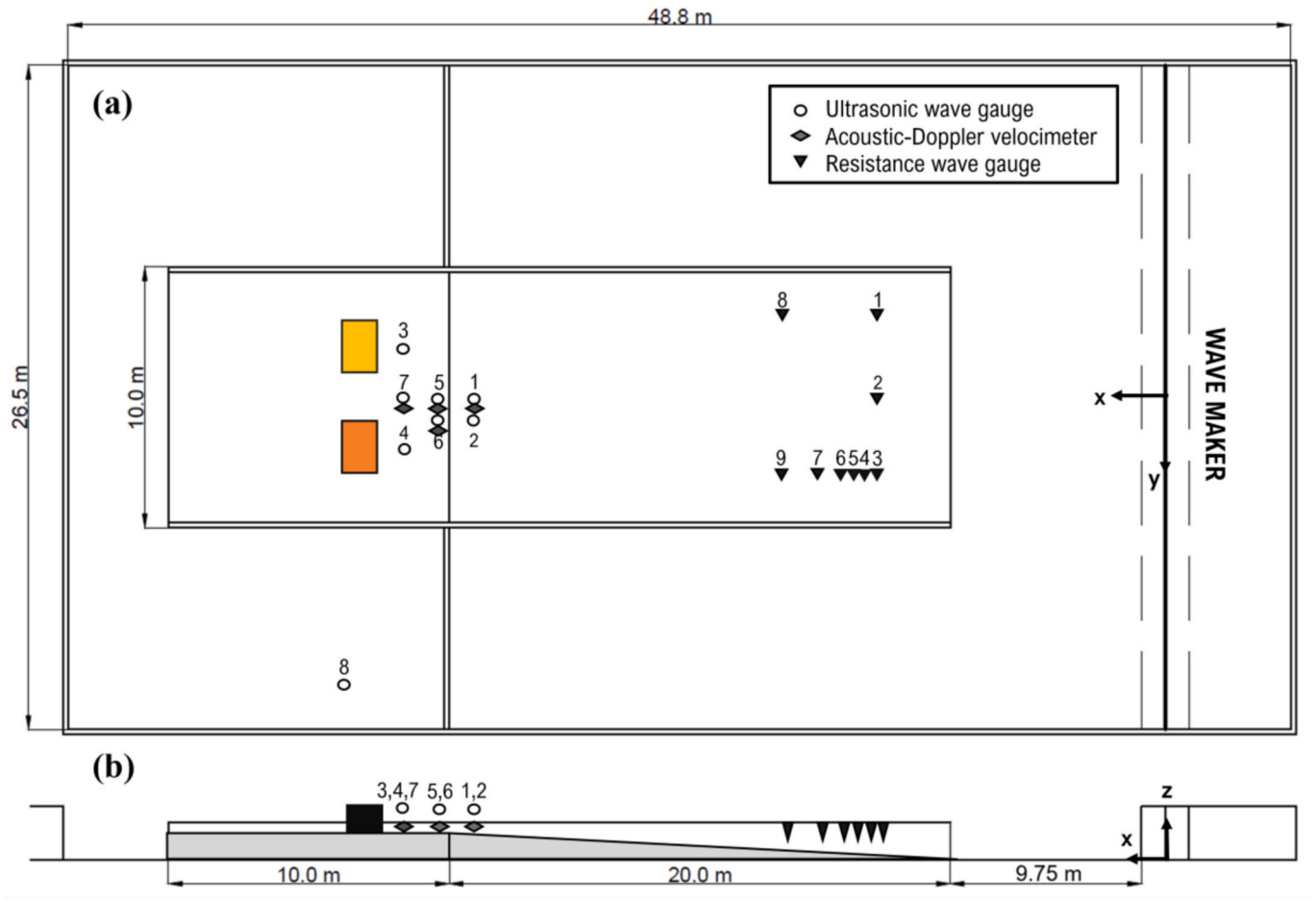

Fig. 1. Schematic of the wave basin setup and instrumentation: (a) plan view; and (b) profile view.

m deep (z-direction) with a multi-directional piston-type wavemaker with 29 individual wave paddles. Each paddle had a max stroke of 2.1 m and a maximum velocity of 2.0 m/s. A 20 m long, 1:20 concrete slope was installed in the basin starting at 9.75 m from the wavemaker, followed by a 10 m long horizontal test section, elevated 1.0 m above the basin's floor. The experimental specimens, two light-frame wooden structures, were positioned on a flat area of 3.5 m from the end of the slope to the wave direction. An on-grade specimen colored in yellow and an elevated specimen colored in orange were firmly installed over the flat test area 3.2 m apart from each other. Here, this numerical study only concentrates on the hydrodynamics of the elevated specimen.

The experiment measured the offshore slope's free water surface elevation through nine wire resistance wave gauges (wg1-wg9). In addition, seven ultrasonic wave gauges (uswg1-uswg7) were installed nearby the specimen, and one of the ultrasonic wave gauges (uswg8) was installed outside of the flat test section. Four acoustic-Doppler velocimeters (adv1, adv5, adv6, and adv7) were placed at the location of four ultrasonic wave gauges (uswg1, uswg5, uswg6, and uswg7) to measure both free surface elevation and corresponding velocity at the same point using the 100 Hz sampling rate. Detailed information is listed in Table 1.

Fig. 2 shows the elevated specimen's detailed dimension and the pressure sensor's location at the bottom of the model. The specimen was initially designed based on the construction detailed in previous research by Burke (2018) and Karny (2018), using a length scale of 1:6. The orange-colored specimen was elevated 0.35 m from the bottom of the testbed with sixteen wooden columns (4 × 4). Each column was nailed to the concrete bottom to withstand uplift forces during the test. Each length and width of the specimen was 1.83 m by 1.22 m, equal to an 11.0 m by 7.3 m prototype (Fig. 2a and b). The model was constructed with the rational scale of openings such as a door and widows used in a typical residential structure. There are two windows on the first floor at the front and back walls of 0.35 m by 0.23 m (length x height), and three windows on the second floor of the front and rear

Table 1
Instruments and their locations for hydrodynamic measurement (From Duncan et al., 2021).

Instrument	data column	*x*(m)	*y*(m)	*z*(m)
Ultrasonic Wave Gauge	uswg1	29.00	0.02	2.29
Ultrasonic Wave Gauge	uswg2	28.99	0.50	2.30
Ultrasonic Wave Gauge	uswg3	32.18	−2.38	2.34
Ultrasonic Wave Gauge	uswg4	32.24	2.47	2.34
Ultrasonic Wave Gauge	uswg5	30.59	0.00	2.36
Ultrasonic Wave Gauge	uswg6	30.58	0.52	2.43
Ultrasonic Wave Gauge	uswg7	32.17	0.04	2.38
Ultrasonic Wave Gauge	uswg8	34.35	12.38	1.84
Resistance Wave Gauge	wg1	14.05	−3.54	n/a
Resistance Wave Gauge	wg2	14.05	−0.06	n/a
Resistance Wave Gauge	wg3	14.04	2.47	n/a
Resistance Wave Gauge	wg4	14.34	2.48	n/a
Resistance Wave Gauge	wg5	14.90	2.48	n/a
Resistance Wave Gauge	wg6	15.39	2.47	n/a
Resistance Wave Gauge	wg7	16.69	2.47	n/a
Resistance Wave Gauge	wg8	19.28	−3.54	n/a
Resistance Wave Gauge	wg9	19.25	2.49	n/a
Acoustic Doppler Velocimeter	adv1	29.02	−0.02	1.02
Acoustic Doppler Velocimeter	adv5	30.59	0.00	1.01
Acoustic Doppler Velocimeter	adv6	30.58	0.48	1.01
Acoustic Doppler Velocimeter	adv7	32.16	−0.12	1.02

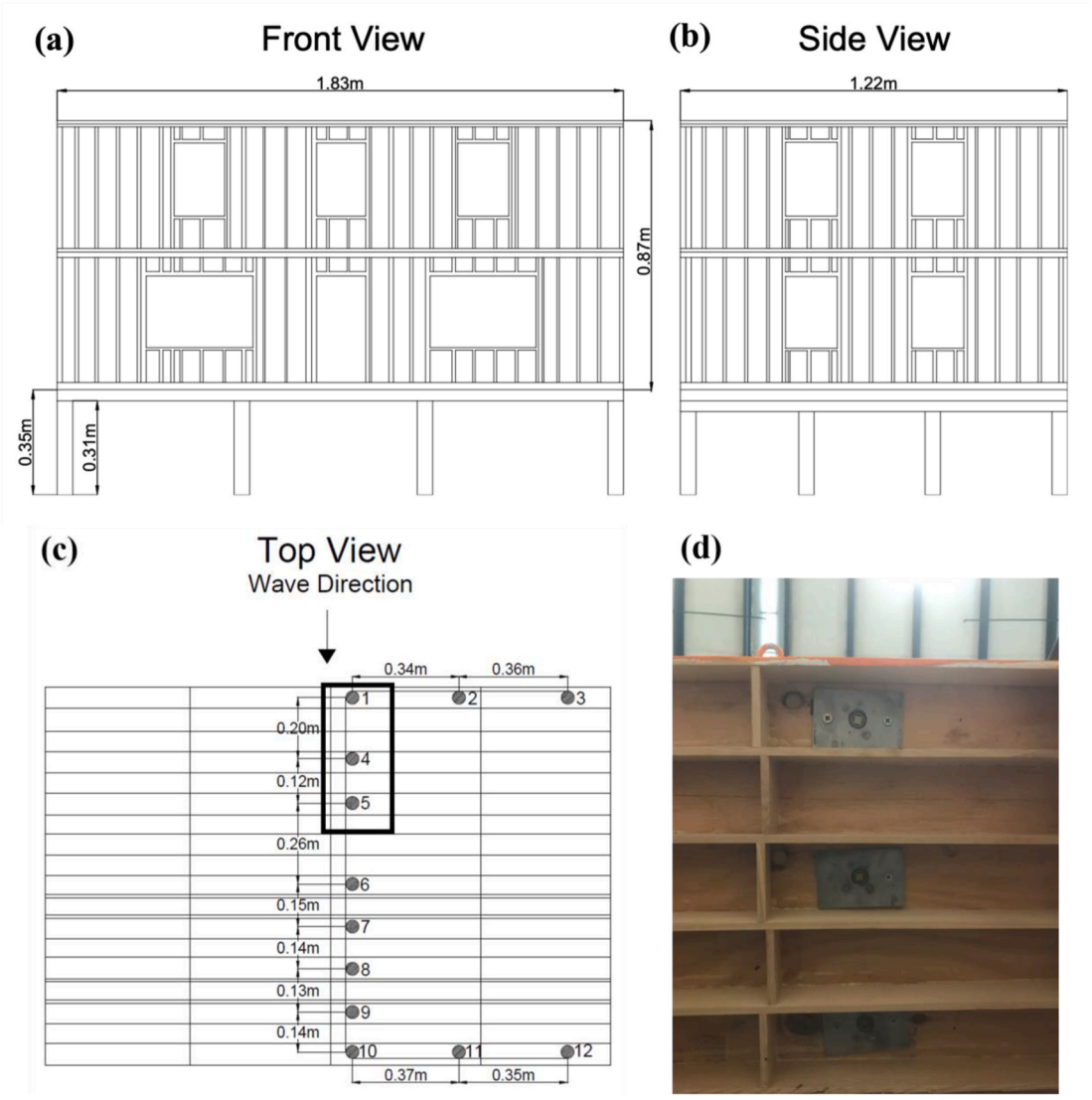

Fig. 2. Specimen and instrumentations: (a) front, (b) side, (c) top view from the ground, and (d) a zoomed in snapshot of pressure sensor 1, 4 and 5 with girders at the bottom of the specimen (inserted black box in Fig. 2c).

walls of 0.17 m by 0.23 m. In addition, there are four windows with 0.17 m by 0.23 m at each sidewall.

A total of twelve pressure sensors were installed on the bottom of the superstructure, facing the bottom between the girders, to acquire the vertical pressure with a 1000 Hz sampling rate (Fig. 2c). Eight pressure sensors (press1, press4 - press10) were positioned along the bottom centerline of the superstructure to measure the uplift pressure to the wave direction (x-direction). Four pressure sensors (press2, press3, press11, and press12) were placed at the right edges of the front and back of the bottom to measure the variation of pressure to the wave's normal direction (*y*-direction). However, none of the pressure sensors are installed in front of the specimen to avoid damage to pressure sensors because the physical experiments (Duncan et al., 2021) were initially designed to quantify the structural responses of the non-rigid body specimen from severe surge and wave conditions till the collapse of the superstructure from the only horizontal force. Therefore, all pressure sensors only measured the bottom pressure (lift pressure) and were secured during the tests (Fig. 2d).

2.2. Experimental wave conditions

Twenty-one trials were performed by changing the water levels and wave heights (Regular waves), and the elevated structure was destroyed in the last trials (Duncan et al., 2021). The physical model used a fixed wave period, T = 4.5 s, except for Trial 09 (T09) and Trial 10 (T10), which were T = 3.5 s and 5.5 s, respectively. Those combinations of surge levels and waves are considered to simulate the scaled Hurricane Sandy's conditions, as noted in Duncan et al. (2021). Each test trial ran for about 3 min to generate a total of forty regular waves. The detailed experiment cases are summarized in Table 2. Water depth, *h,* is the net flow depth at a flat section (1.0 m above the basin floor), ranging from 0.1 m to 0.45 m, and the input wave heights, H, range from 0.1 to 0.4 m. The air gap, a, is the distance from the bottom of the superstructure of the specimen relative to the still water level. The negative values in the air gap are measured when the superstructure is submerged from a still water level. The modified air gap, a' which is listed in the 4th column in Table 2, is adapted to consider a 4 cm height of the exterior girder installed at the bottom of the superstructure (Fig. 2a). Besides 21 trials in the physical experiments, additional five tests (N01 – N05) were not performed in physical model studies due to temporal and equipment limitations in the experiment but numerically simulated using the olaFlow model for this study.

Table 2
Water levels, input wave conditions, and breaking type for all trials.

Trial number	h (m)	a (m)	a' (m)	H (m)	T (s)	*Breaking type	Notes
T01	0.10	0.25	0.21	0.10	4.5	Broken	
T02	0.10	0.25	0.21	0.40	4.5	Broken	
T03	0.12	0.23	0.19	0.10	4.5	Breaking	
T04	0.20	0.15	0.11	0.20	4.5	Broken	
T05	0.20	0.15	0.11	0.30	4.5	Broken	
N01	0.25	0.10	0.06	0.20	4.5	Breaking	Only numerical
N02	0.25	0.10	0.06	0.30	4.5	Broken	Only numerical
N03	0.25	0.10	0.06	0.40	4.5	Broken	Only numerical
T06	0.30	0.05	0.01	0.10	4.5	Nonbreaking	
T07	0.30	0.05	0.01	0.20	4.5	Breaking	
T08	0.30	0.05	0.01	0.30	4.5	Broken	
N04	0.30	0.05	0.01	0.40	4.5	Broken	Only numerical
T09	0.30	0.05	0.01	0.30	3.5	Broken	
T10	0.30	0.05	0.01	0.30	5.5	Broken	
T11	0.35	0.00	−0.04	0.10	4.5	Nonbreaking	
T12	0.35	0.00	−0.04	0.20	4.5	Breaking	
T13	0.35	0.00	−0.04	0.30	4.5	Broken	
T14	0.35	0.00	−0.04	0.40	4.5	Broken	
T15	0.40	−0.05	−0.09	0.10	4.5	Nonbreaking	
T16	0.40	−0.05	−0.09	0.20	4.5	Breaking	
T17	0.40	−0.05	−0.09	0.30	4.5	Breaking	
T18	0.40	−0.05	−0.09	0.40	4.5	Broken	
T19	0.45	−0.10	−0.14	0.10	4.5	Nonbreaking	
T20	0.45	−0.10	−0.14	0.20	4.5	Nonbreaking	
T21	0.45	−0.10	−0.14	0.30	4.5	Breaking	
N05	0.45	−0.10	−0.14	0.40	4.5	Broken	Only numerical

3. Numerical model: OpenFOAM

The numerical simulations were performed with the open-source CFD toolbox, OpenFOAM (with version 5.0), written in C++ programming language (OpenCFD, 2017), which numerically solves three-dimensional Reynolds Averaged Navier-Stokes (RANS) equations to calculate the hydrodynamics on the elevated structure under varied wave conditions. The RANS equations have the advantage of allowing various determinations such as the characteristics of turbulence generated in the wave breaking zone, the resulting waves' impacts on coastal structures, and the simulations of simultaneous hydrodynamic and aerodynamic flow. OpenFOAM allows using the finite volume method (FVM) with structured or unstructured 3D meshes, and the computational domain is sectioned into a finite number of cells. Flow variables are calculated at the centroid of each control volume. The structure of OpenFOAM also allows the applications to pre-and post-process the cases, including mesh generation tools (blockMesh, snappyHexMesh) and visualization (ParaView). OpenFOAM uses Message Passing Interface (MPI) protocol for parallel computing works, which can be decomposed into a user-defined sub-domain.

In this study, we utilize olaFlow [http://doi.org/10.5281/zenodo.1297012], a wave modeling package, and the latest advances for wave modeling further developed from IHFOAM (Higuera et al., 2013a), which is developed based on OpenFOAM platform and com piled with interFoam solver to solve incompressible, multiphase hydrodynamics. olaFlow (Higuera et al., 2015) contains boundary conditions to actively generate and absorb the waves and supports boundary conditions for a piston and flap-type wave paddle generation. Therefore, a sponge layer or relaxation zone was not used to reproduce the physical experiment setup.

3.1. Governing equations

The numerical model solves the three-dimensional RANS equations to describe the flow kinematics and dynamics. The Volume of Fluid (VOF) method is applied to simulate two-phase (water and air) immiscible fluids and identify a free surface configuration. The VOF method depends on the fact that air and water are not interpenetrating, defining a variable α, which provides a fractional volume of water in each of the two fluids in the cell. The range of α is from 0, at the volume is occupied by air ($\rho_{air} = 1.20\ kg/m^3$, $\nu_{air} = 1.48\ \times 10^{-5} m^2/s$), to 1, at the volume is occupied by water ($\rho_{water} = 1.0 \times 10^3\ kg/m^3$, $\nu_{water} = 1.0\ \times 10^{-6} m^2/s$). Here, density, ρ is the mass density of the fluid (air or water) and ν is the kinematic viscosity. Based on the value of α, each control volume in the domain is assigned suitable properties and variables.

$$\alpha = \begin{cases} 0 & in\ air \\ 0 < \alpha < 1 & in\ the\ interface\ cell \\ 1 & in\ water \end{cases} \tag{1}$$

The air-compression is not considered in the model governing equation based on the incompressible flow assumption. The RANS equations including conservation equations with the assumption of incompressible fluid conditions are shown below:

$$\frac{\partial u_i}{\partial x_i} = 0 \tag{2}$$

$$\frac{\partial \rho u_i}{\partial t} + \frac{\partial \rho u_j u_i}{\partial x_j} - \frac{\partial}{\partial x_j}\left(\mu_{eff}\frac{\partial u_i}{\partial x_j}\right) = -\frac{\partial p^*}{\partial x_i} - g_j x_j \frac{\partial \rho}{\partial x_i} \tag{3}$$

Here, each u_i x_i, and g_j is the velocity, position, and gravity component in the Cartesian coordinate system, respectively, and each μ_{eff} and p^* is the effective dynamic viscosity, which includes the molecular dynamic viscosity with turbulent effects: $\mu_{eff} = \mu + \mu_{turb}$ and the dynamic pressure. The dynamic pressure (p^*) is defined as $p - \rho g_i x_i$. The density (ρ) is calculated as $\rho = \alpha\rho_{water} + (1 - \alpha)\,\rho_{air}$, where α represents the phase fraction, given by Eq. (4):

$$\frac{\partial \alpha}{\partial t} + \frac{\partial}{\partial x_i}(u_i \alpha) + \frac{\partial}{\partial x_i}\left(u_i^r \alpha(1-\alpha)\right) = 0 \tag{4}$$

In Eq. (4), u_i^r indicates the compressive velocity component (Berberović et al., 2009) for preserving a sharp interface. The term $\frac{\partial}{\partial x_i}(u_i^r \alpha(1-\alpha))$ is an extra artificial compression term to keep α be conserved and bounded between 0 and 1 (Rusche et al., 2002). This term is different from 0 only at the interface due to the $\alpha(1-\alpha)$ factor and u_i^r is defined by Eq. (5):

$$\left|u_i^r\right| = \min\ (C_\alpha |\overline{u_i}|\ at\ x_i,\ \max(|\overline{u_i}|)\forall\ x_i\ )\ \text{at a free surface} \tag{5}$$

here, C_α is a user specified coefficient, which is equal to 1 as a default value (Higuera et al., 2013a; Maza et al., 2015). It is worthy to note that the term compressive velocity is not directly related to the compressible flow.

olaFlow utilizes the PIMPLE algorithm as a default solver for the incompressible, transient, and turbulent flow. The PIMPLE algorithm is the coupling model between SIMPLE (Semi Implicit Method for Pressure Linked Equations) and PISO (Pressure Implicit with Splitting of Operators) to solve the RANS equations. In our study, the input wave conditions are unsteady and require time-marching solutions except the initial warm-up stage. Therefore, the PISO algorithm would be utilized in most model calculation, while the SIMPLE algorithm is locally applied to accelerate the model calculation under the relaxing condition.

3.2. olaFlow model setup

The numerical model duplicated the 1:6 scale experimental tests including all detailed exteriors surface of the specimen including windows and doors. Initially, we utilized the symmetric model (a half of the specimen) to reduce computation time, but it caused minor deviations during the model validation. Particularly, the time-series surface elevation at WG1, 5, and 7 showed minor deviations as those gauges locates between the elevated structure (orange) and slab on grade structure (yellow) in Fig. 1. Therefore, we utilized the wider lateral wall conditions in our numerical model study. The numerical domains reduced from 48.8 m to 41.7 m in length (x-direction) by installing wave absorbing boundary, and from 10 m to 6 m in width (y-direction) to simulate the area for the elevated specimen. It is noted here that the physical model studies (Duncan et al., 2021) performed both elevated and slab on grade specimens at once, and each specimen was in parallel across the 10 m width. The effects of shortening the lateral domain of the numerical wave basin were negligible because the physical experiment originally installed two buildings (elevated and on-grade specimens) parallel. Also, the specimen is 0.35 m elevated; thus, the actual blockage ratio (e.g., Qi et al., 2014) would be less than 10% in our numerical model study. In addition, it was not necessary to design the space from the back of the specimen to the end of the basin because olaFlow supports a reflective wave control function.

The numerical mesh setup for the elevated specimen was shown in Fig. 3, which describes the three-dimensional view and numerical domain with mesh size. The resolution of meshes in the computation domain affects not only the computation time but also the accuracy of flow dynamics. Therefore, the optimized mesh configuration is applied using varied mesh sizes from 10 cm in the offshore region to 0.8 cm near the specimen, as shown in Fig. 3b and c.

If the shape of the field is simple, the grid can be defined through an ASCII text editor in the blockMesh tool, which creates the geometry by defining vertices, faces, and boundary of each block. However, in the complex case, it may be required to create a non-aligned or variable grid. In that case, additional work requires to create geometric data using STL (STereo Lithography) files and utilize the snappyHexMesh tool. In this study, the specimen with a 1:20 slope was created by snappyHexMesh after the box-type boundary of the three-dimensional basin was set up using the blockMesh tool. The numerical domain contained only the elevated specimen section and the location of ultrasonic wave gauges 1, 4, 5, and 7 (Figs. 1 and 3). The total number of the grid elements was about 5,060,000, and the detailed mesh setup to the specimen is shown in Fig. 4.

The summary of boundary conditions is listed in Table 3. olaFlow allows to use a set of boundary conditions for wave generation and absorption. In this study, we assign the wave generating boundary on the offshore wall and wave absorbing boundary at the onshore wall. Here, *Inlet/outlet* indicates the wall for wave generating and absorbing, respectively. *All walls and floors* indicate cross-shore side walls, bottom walls including the slope in the numerical wave basin, and all specimen surfaces. We assign the solid wall conditions for *All walls and floors*. The last term, *atmosphere*, is the upper boundary of the numerical computational domain. More details of numerical fields and boundaries

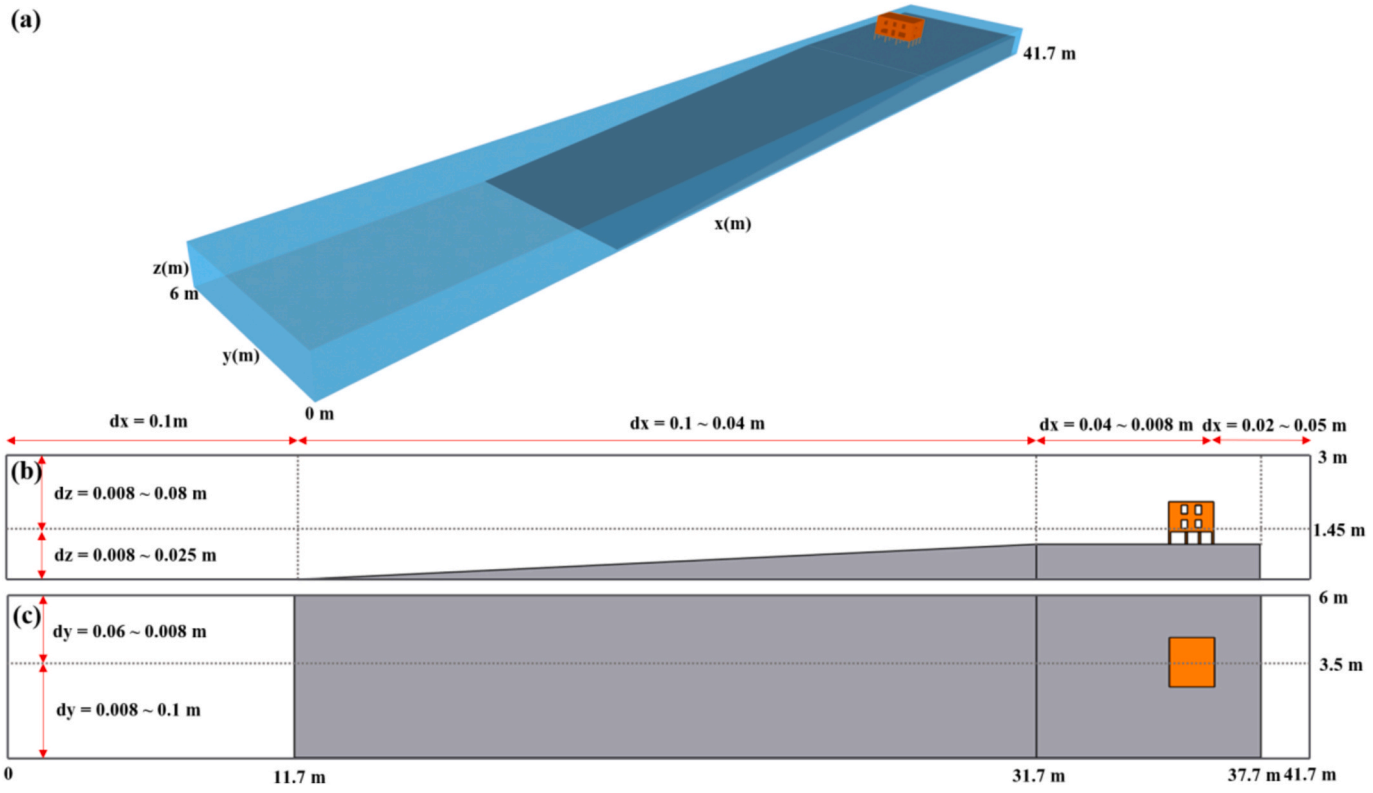

Fig. 3. (a) 3D sketch of wave basin with the elevated specimen in the olaFlow model and the mesh configuration for (b) side and (c) top view.

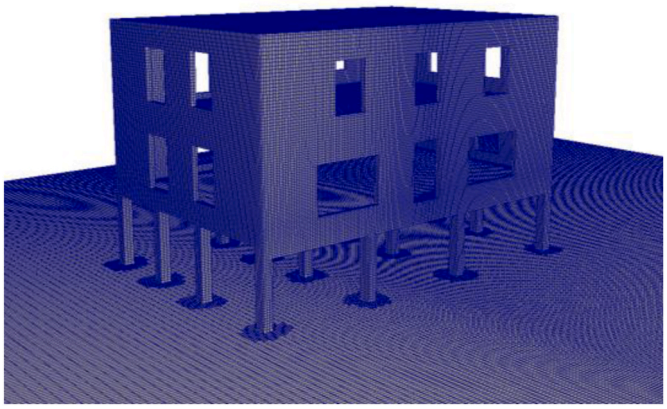

Fig. 4. Zoomed in the mesh of the elevated specimen and testbed.

applied in this study are available from the User Guide of OpenFOAM. (https://www.openfoam.com/documentation/user-guide).

The active wave absorbing boundary is set at the onshore boundary to effectively absorb outgoing waves (Higuera et al., 2013a). The active absorbing boundary utilizes a linear shallow water equation to predict the velocity at the onshore boundary. The reflected portion is estimated and adapted in the wave-maker to generate the target wave precisely considering the reflection. The previous works from Higuera et al. (2013b); Higuera et al. (2015) successfully tested the applications of wave generation in olaFlow for regular and irregular waves according to several wave theories; Stokes I, II, and V, Cnoidal and stream function regular waves; Boussinesq solitary wave; irregular (random) waves, first and second-order; and piston-type wavemaker velocity profile replication. The signal of time, paddle velocity, and paddle eta are necessary to generate the wave input using the measured real-time signal. Wave generation can also be conducted using the waves2Foam solver, which also provides utilities to generate and absorb surface waves by applying the relaxation zone.

Turbulence is a complicated and significant phenomenon in hydraulic engineering problems and there are many turbulence closure models including $k-\varepsilon$, *RNG* $k-\varepsilon$, and $k-\omega-SST$ for representatively. A hybrid of $k-\varepsilon$ and $k-\omega$ models known as the Shear Stress Transport (SST) $k-\omega$ model was introduced by Menter (1993), where the area between the wall and extent of the boundary layer is calculated using the $k-\omega$ model, while the $k-\varepsilon$ model for the area outside this region. In this study, we chose the k−ω−SST as the turbulence model following the previous numerical studies of the author (Park et al., 2018). In general, the k−ω−SST is known as stable and leads to better performance in swash zone and near-wall regions, where the flow is partially separated and broken (e.g., del Jesus et al., 2012; Higuera et al., 2013; Liu et al., 2020).

A small Courant Number, less than the unity, is recommended for model stability in the numerical model. We set the Courant Number from 0.5 to 0.7 by considering different wave hydrodynamic conditions, following the previous numerical model studies of elevated structures using OpenFOAM from Park et al. (2018). The total simulation time of the T12 was 96 h for 55 s in the model with 2.6 GHz Intel Xeon Gold 6 240 machines with a 21-core parallel. The actual simulation time is ranged 48 h to 144 h depending on wave and depth conditions.

4. Validation of numerical models

In this section, we quantitatively compare our model results to the physical model results to validate the numerical model. Fig. 5 shows both snapshots of the numerical simulation and physical experiment of T12 (H = 0.2 m, h = 0.35 m, and a = 0 m). Each panel shows a series of snapshots from olaFlow simulation and recorded videos from the physical experiment at three-time steps, including the moment of wave impact on the specimen (Fig. 5b, e, and h) and just before (Fig. 5a, d, and g) and after (Fig. 5c, f, and i) the wave impact, respectively. Each color in the snapshot represents the magnitude of the wave velocity at a reference direction. The red color indicates the positive x-directional velocity in Fig. 5a, b, and c. Similarly, the red color indicates the positive y-directional velocity from right to left in Fig. 5d, e, and f.

We can observe the significant inflows to the structure through both front and side openings at the time of wave impact (Fig. 5b and e) but outflows through the openings after the wave impact (Fig. 5c and f). These abrupt changes in flow fields inside the structure could not be observed in the solid box-shaped elevated structure (Park et al., 2017; Park et al., 2018) and alter hydrodynamic conditions. The openings on the elevated structure may play a significant role in reducing the impact loadings (e.g., Wilson et al., 2009) but may cause damage to the inside frames. However, the current study couldn't focus on capturing details of pressure fields inside the structure. Still, the detailed change of hydrodynamics inside and outside of the elevated structure needs to be studied to understand better the damage process on the elevated structure under extreme wave conditions.

For quantitative model validation, we compare the time series of free surface water elevation, velocity, and pressure loading on the specimen between numerical and physical models. A total of three ultra-sonic wave gauges (uswg4, uswg5, uswg7) and a wire resistance wave gage (wg9) for water surface elevations and three ADVs (adv1, adv5, adv7) for horizontal and vertical wave velocities and eight pressure gauges (press1, press4, press5, press6, press7, press8, press9, press10, measured at the bottom face of the specimen, are compared to numerical model results. Each position of uswg and ADV was provided in Fig. 1a, and pressure was shown in Fig. 2c. The numerical model validation performs with three distinct wave breaking conditions, such as nonbreaking (T11), breaking (T12), and broken (T13) wave conditions.

4.1. Nonbreaking wave (T11)

The model validation results of the free surface elevation at the nonbreaking wave condition (T11) is shown in Fig. 6. The water depth of T11 is 1.35 m at the wave maker, and it provides 0.35 m net water depth at the specimen after the slope as shown in Fig. 1b. The regular wave height (H) of T11 is 0.1 m at the wavemaker, and we couldn't observe any breaking waves from physical and numerical models. Therefore, we classified the T11 as the nonbreaking wave condition. Each Fig. 6a, b, 6c, and 6d shows the time-series of surface water elevation at wg9, uswg5, uswg7, and uswg4, which posed from the offshore to the onshore (Fig. 1a). Each black solid and red dotted lines indicate the physical model results and numerical model result, respectively. As waves propagate over the slope from the wavemaker toward the specimen, the shapes of the waveform grew steeper from wg9 to uswg7, and the wave height increases due to the shoaling effect. Particularly, uswg4 and uswg7 were located at the exact long-shore location (x) but the different cross-shore locations (y). We can measure the reflected wave

Table 3
Numerical model (OpenFOAM) boundary conditions.

Numerical field, variable	*Inlet/outlet*	*All walls and floors*	*Atmosphere*
Air/water phase, α_{water}	waveAlpha/zeroGradient	zeroGradient	inletOutlet
Velocity, U	waveVelocity/waveAbsorption	no-slip	PressureInletOutletVelocity
Pressure without hydrostatic part, p_{rgh}	fixedFluxPressure	fixedFluxPressure	totalPressure

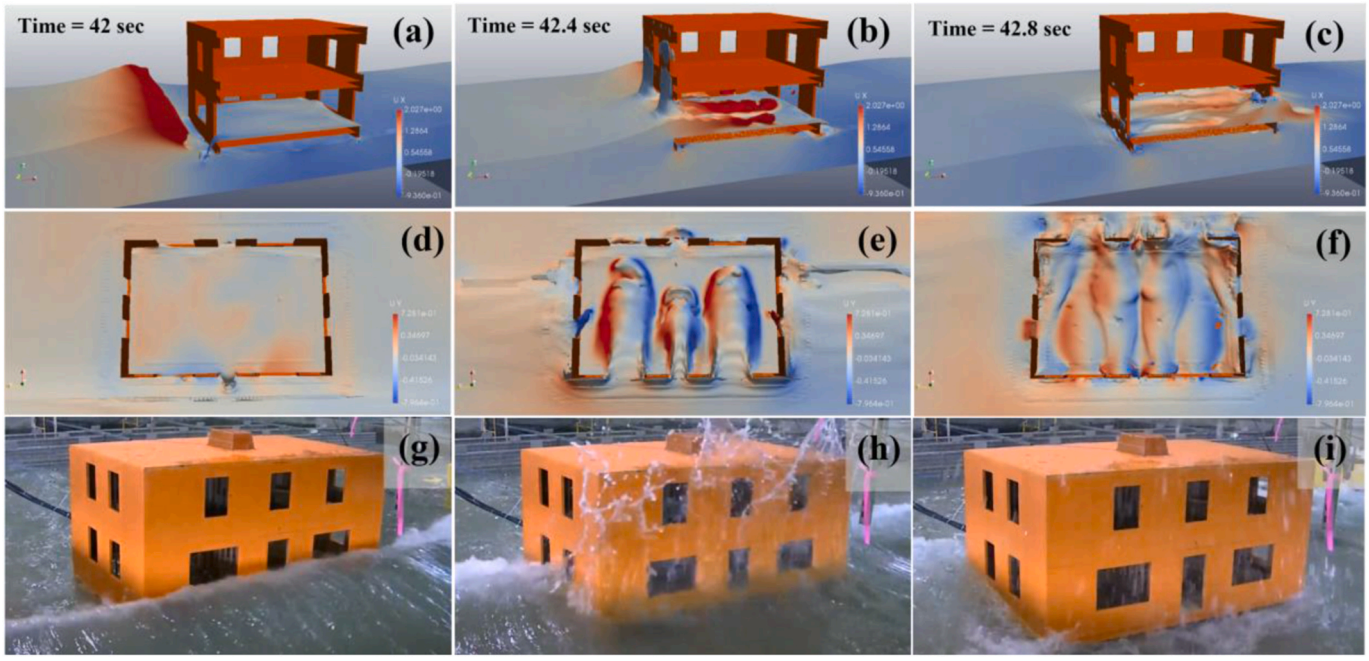

Fig. 5. Snapshots of the numerical model simulation colored by the x-directional velocity at continuous time steps (a–c), y-directional velocity (d–f) inside the first floor of the structure, and synchronized images from the experiment (T12, breaking wave condition). The mesh grid of the structure was cut in half vertically (a–c) and horizontally (d–f) to check the fluid flow inside the structure in the simulation tool.

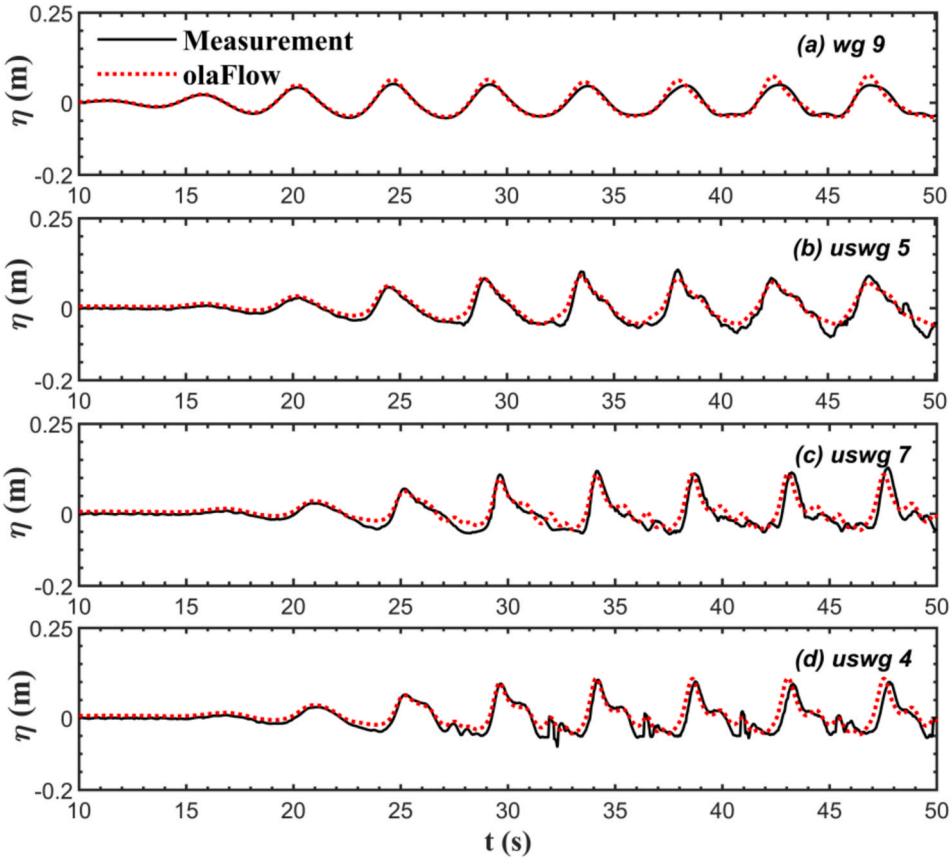

Fig. 6. Numerical model comparison results of water surface elevation for nonbreaking wave condition, T11. Experiment (black solid line) and olaFlow (red dotted line).

components from the specimen and wave-structure interaction in uswg 4 (Fig. 6d), which is captured in both physical and numerical results. Still, the wave trough was not captured clearly, and the phase is slightly shifted in the numerical model results. Those differences may come from the mesh resolution, or a rigid body assumption used in the numerical model.

Fig. 7 shows the model comparison results of horizontal (x-component) and vertical (z-component) wave velocities at the nonbreaking wave condition. Each group of Fig. 7a and b, Fig. 7c and d, and Fig. 7e and f presents the time series of horizontal and vertical velocity at adv5, adv6, and adv7, respectively. Overall, horizontal velocity in numerical model results shows good agreement with the experimental model results before t = 35 s. However, we can observe slightly deteriorated after t = 35 s, and the numerical model started overestimating the horizontal velocities (Fig. 7a and c). Those discrepancies may be generated from the incomplete wave absorption in the physical model after the specimen (Duncan et al., 2021), while the numerical model excluded reflection effects through the wave absorbing boundary at the outlet. Vertical wave velocity is not the primary physical value in this study, but we also confirm that this value is well verified in numerical models. The variation in vertical velocity is relatively apparent in adv5 (Fig. 7b and d) but not in adv7 (Fig. 7f). Some negative peak values occurred in adv7 (Fig. 7f), but nothing was detected in numerical model results.

Fig. 8 shows the numerical and physical model comparisons of bottom pressure (up-lift pressures) for the nonbreaking wave condition at press1(a), press4(b), press5(c), press6(d), press7(e), press8(f), press9(g),

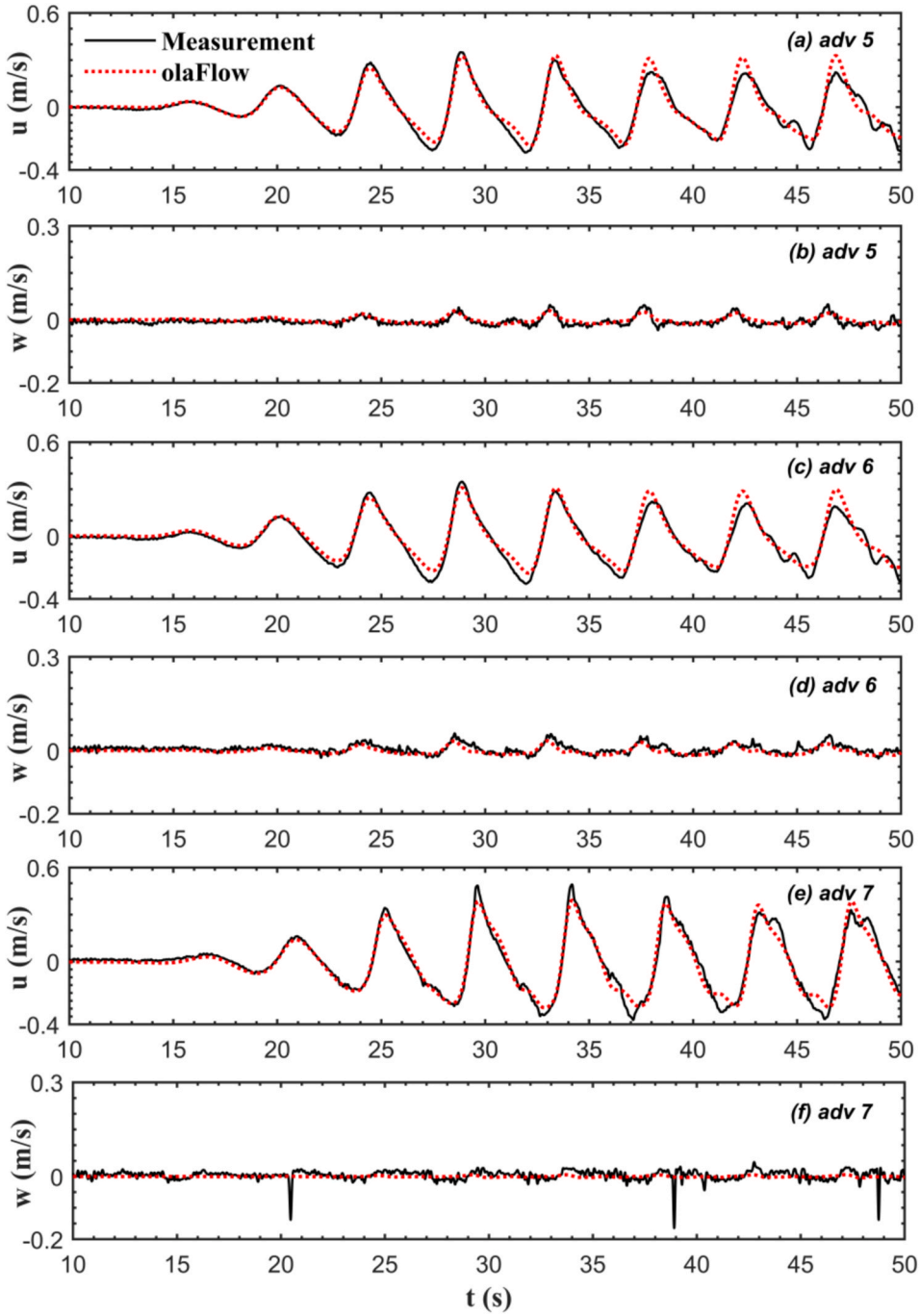

Fig. 7. Numerical model comparison results of horizontal (u) and vertical (v) wave velocities for nonbreaking wave condition at T11. Experiment (black solid line) and olaFlow (red dotted line).

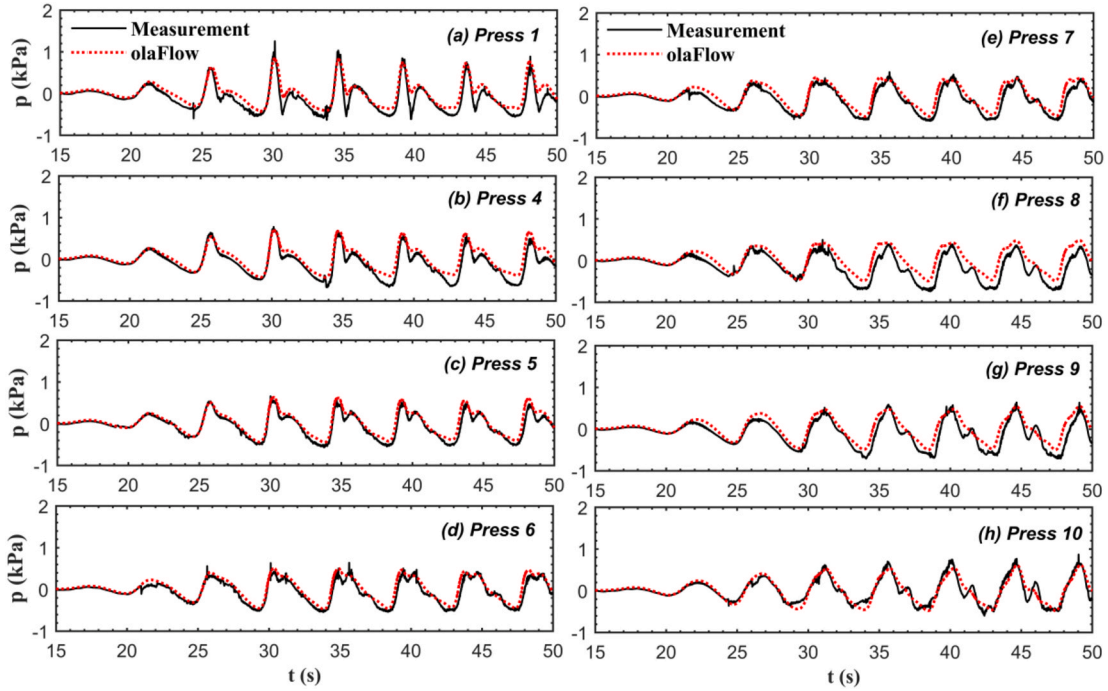

Fig. 8. Numerical model comparison results of vertical pressures at the bottom of the specimen for nonbreaking wave condition, T11. Experiment (black solid line) and olaFlow (red dotted line).

and press10(h). In general, numerical model results match well with the measured pressure data from the experiment, including the quantity of the peak pressure and shapes, but slightly overestimated at the trough in press1, 4, and 8.

4.2. Breaking wave (T12)

The model validation results of water surface elevation, horizontal wave velocities, and the vertical pressures for the breaking wave conditions (T12) are shown in Fig. 9. Each Fig. 9a and b shows the model validation of the free surface elevation at uswg4 and uswg7, which are the wave gauges located mostly near the specimen. In addition, the model validation of the horizontal wave velocities (x-directional component) at adv5 (Figs. 9c), and 7 (Fig. 9d) and bottom pressures at press1 (Fig. 9e), press5 (Fig. 9f), press7 (Fig. 9g), and press9 (Fig. 9h) are presented. Overall, the simulated results show an excellent agreement with the measurement data. However, a similar discrepancy was found at uswg4 that the numerical model results underestimate the surface

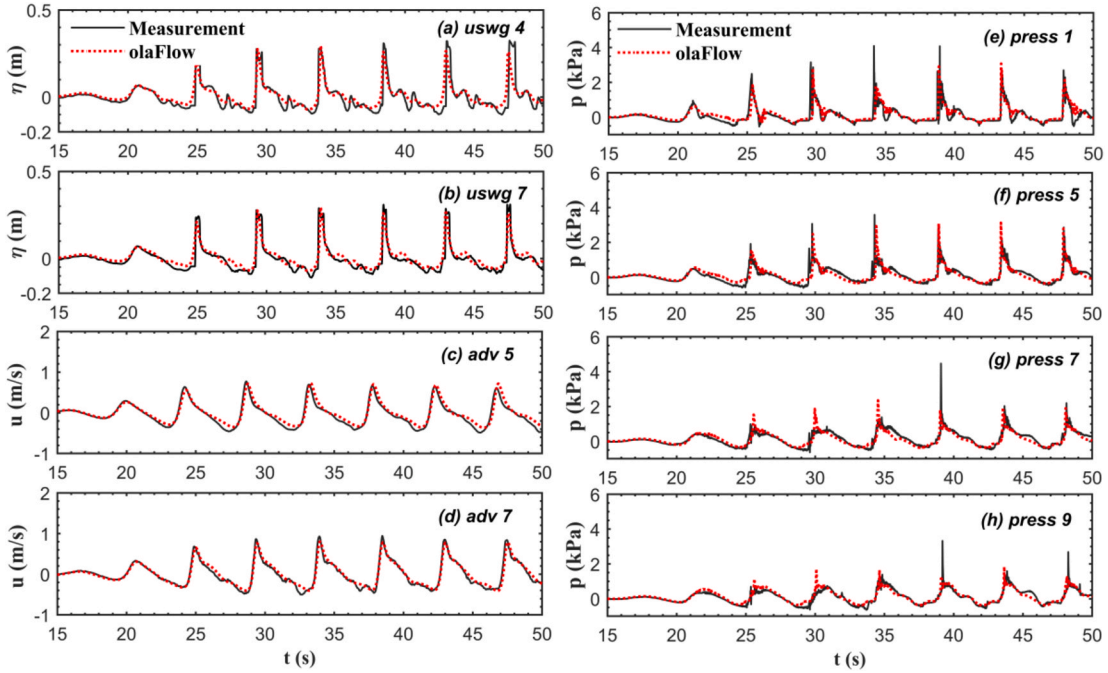

Fig. 9. Numerical model comparison results of water surface elevation (a, b), horizontal wave velocities (c, d), and bottom pressures (e, f) for breaking wave condition, T12. Experiment (black solid line) and olaFlow (red dotted line).

elevation, and the phase is shifted after t = 35 s (Fig. 9a). As for the bottom pressures, Fig. 9e–h shows good agreement between the wave pressures given in the numerical model and measured in the physical model. Typically, the overall shape of time series pressure including the magnitude and phase of the numerical model well-matched with the measurements except for the peaky pressures at press7 and press 9. Those peaky impulsive pressures at the wave impact are not captured in the current model setup. While peak pressures are mostly insensitive to calculating the total forces at the current model and previous works on the elevated structure model studies. (Park et al., 2017, Park et al., 2018). The future numerical modeling for those peaky pressure is suggested to simulate with a refiner mesh or smaller computation time step using a smaller Courant number (current Co ~ 0.5) and consider the effects of air-compressibility in model calculation.

4.3. Broken wave (T13)

Fig. 10 shows the same comparison format as Fig. 9 but for the broken wave condition (T13). The predicted and measured time-series of water surface elevations, η, for uswg4 and 7 (Fig. 10a and b), cross-shore (x-directional) velocities for adv5 and 7 (Fig. 10c and d), and bottom pressures for press1, 5, 7, and 9 (Fig. 10e −10h) are compared. Like other breaking types, the numerical model results show good agreement with the measured data. Still, the overall phase of the numerical model is slightly faster than the experimental results after 35 s. In the water surface elevation, the measurements are more stable after t = 35 s. A good agreement is observed for the wave velocity results (Fig. 10c and d), with a slight discrepancy in the wave trough amplitude. Like the breaking wave conditions, the peaky pressure at press5 and 7 in the experimental data were not sufficiently generated in the numerical model.

4.4. Vertical forces using pressure integration

The physical experiments measured the wave-induced vertical pressures at 12 pressure sensors located bottom of the superstructure above 0.35 m from the flat ground. Those pressure sensors data were utilized to calculate the lift force using spatial integration of each sensor. Fig. 11a shows the comparison results of vertical force the directly integrated pressure from pressure sensors (solid black line) versus two of numerical modeling results: the one using the same pressure integration from the numerical model results (solid blue line) and the other is directly calculated from the numerical model using all the mesh points at the bottom of the specimen (red dotted line).

For better analysis of the vertical force from a regular wave condition, we take an ensemble average of the last five wave-induced forces, excluding the first three transient waves before reaching the target wave condition (29 s < t < 51 s in Fig. 11a). Although the time of peak force was slightly different, the ensemble-averaged peak vertical forces show good agreement between physical and numerical model results. Overall, the numerical result overestimates about 6.6% of the peak value of the vertical force at the breaking wave conditions, T12 (Fig. 11b). Similarly, we confirmed that each numerical result of nonbreaking (T11) and broken (T13) wave case underestimates 5.3% and overestimates 7.8% of the peak value of the vertical forces. Even though the numerical model could not accurately reproduce all the peaks of single waves that occurred in the experiment, the deviation of the ensemble-averaged peak at the three different wave conditions dropped to less than 8%. Therefore, we utilize the ensemble-averaged horizontal forces to evaluate the horizontal loading conditions on the elevated structure in the next section. Also, the numerical results of ensemble averaged vertical force in nonbreaking (T11) and broken (T13) wave case are shown in the appendix figure (Figure A1), and overall data including ensemble averaged wave heights, horizontal and vertical forces from numerical model are provided in the appendix table (Table A1).

5. Simulation results

5.1. Pressure distribution on the front face of the specimen

In Figs. 12 and 13, we evaluate the distributions of wave-induced horizontal pressure on the elevated structures under varied air gap (water level) and wave conditions. We extract a total of 16 pressure data points from the numerical model results along the vertical line, between the center and left window on the front face of the specimen, as shown in the inserted Fig. 12a. In Table 1, we already defined z for the elevation of

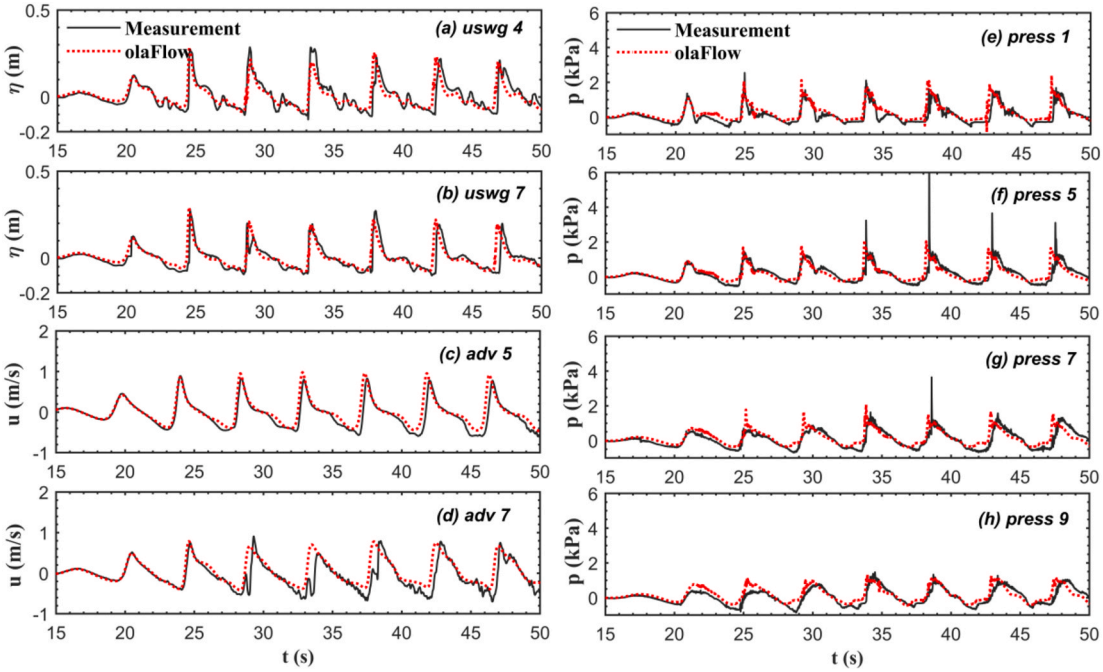

Fig. 10. Numerical model comparison results of water surface elevation (a, b), horizontal wave velocities (c, d), and bottom pressures (e, f) for broken wave condition, T13. Experiment (black solid line) and olaFlow (red dotted line).

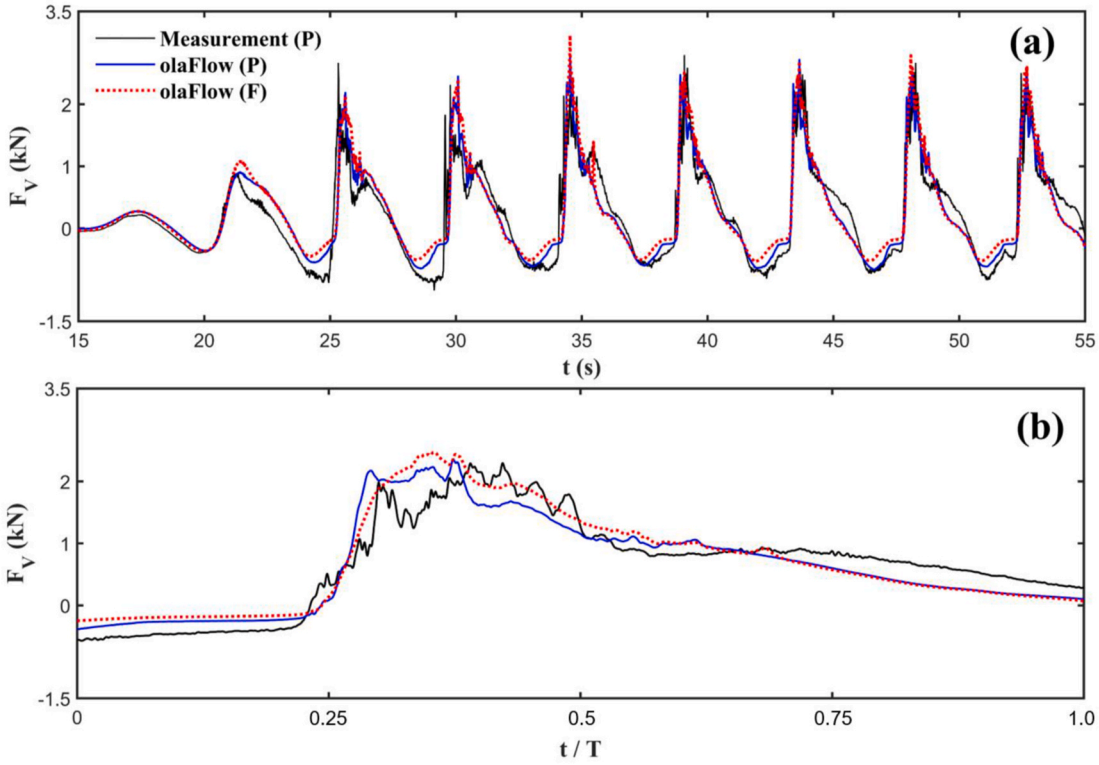

Fig. 11. Comparisons of the vertical forces obtained by three different methods at T12. (a): The integration of the bottom pressure from the experiment (black solid line), the integration of the bottom pressure from the numerical model (blue solid line), and the acquisition directly in the numerical model (red dotted line). (b): Ensemble averaged vertical forces.

measurement devices, including the flat test depth of 1 m. Therefore, z' which is the height from the flat test region is newly defined as z' = z - 1.0 (m) in this section. The lowest pressure data point is at z' = 0.32 m, and the highest pressure data point is at z' = 1.13 m. The distance of each data point was set 2 cm distance at the first floor where the wave hit the specimen (z' = 0.3 m–0.5 m) and about 10 cm above the second floor. Each Fig. 12a, b, 12c, and 12d show the dimensionless maximum horizontal pressure profile at different water levels, which are z' = 0.3 m, 0.35 m, 0.4 m, and 0.45 m, respectively. Here, the maximum pressure is normalized using the dynamic pressure term, $\rho g\overline{H}$, where ρ is the water density (1000 kg/m^3), g is the gravitational acceleration (9.81 m/s^2), and $\overline{H}$ is the ensemble-averaged wave height following Fig. 11b. We utilize wave height at uswg7 for nonbreaking wave cases and uswg5 for breaking and broken wave cases to avoid the effects of direct reflected waves.

At four water levels, we compare the three-wave breaking conditions (nonbreaking, breaking, and broken). As we described in Table 2, we classified T06, T11, T15, and T19 as the nonbreaking wave conditions (grey circle), T07, T12, T16, and T21 as the breaking wave conditions (yellow hexagram), and T08, T13, T18, and N05 as the broken wave conditions (sky diamond). Here, a horizontal red dashed dot line indicates the free surface water level at each figure. We also compared our numerical peak pressure distribution with the empirical dynamic pressure for a wall structure that the dynamic pressure increased linearly from zero at the upper limit to the maximum pressure value and then decreased linearly from the maximum value to zero at the toe of the wall (Fema, 2011; Walton et al., 1989). The maximum pressure value was defined as $P_{max} = 1.6wh$. Here, w is the unit weight of seawater (640 lb/ft^3), and h is the flow depth in feet. We calculated the pressure distributions (dotted lines) for four different water level, h = 0.30, 0.35, 0.40, and 0.45 m, and truncated the pressures to display the pressure at the frontal face of the elevated structure. The dotted lines in Fig. 12 are normalized pressure distribution. We picked the breaking wave height to normalize the results to compare with the breaking wave pressure condition in the numerical model because the maximum force and pressures are developed in the breaking wave condition.

In the case of nonbreaking wave conditions, the peak pressure value is mostly found near the still water level (red dashed line) except T06. Overall, the maximum pressure values at each point decreased significantly above the water level while it decreased moderately below the water level. This pattern is shown clearly in all nonbreaking wave condition. Likewise, the broken wave condition also shows the peak pressure value near the still water level, but the pattern of pressure distribution was irregular (Fig. 12b). To specific, the broken case (T13) had lower vales than the breaking case (T12) above 0.4 m, but a sharply intense pressure appeared as it approached 0.35 m, which is the water level. Moreover, T18 (Fig. 12c) had two peaks in the distribution. The other peak in the upper part could come from the air pocket generated by the wave hitting the front specimen in the broken state. Lastly, it was confirmed that the breaking cases had a maximum value in the vicinity of 0.05–0.1 m above the still water level.

The general pattern of the pressure distribution from the empirical equation shows a similar shape to the numerical model results. Both results showed the maximum pressure near the still water level and decreased to the upper and lower limits. However, the linear pressure distributions significantly underestimate the numerical model's pressures.

In Fig. 13, we re-group and plot Fig. 12 a normalized maximum pressure distribution at three-wave breaking conditions. Each Fig. 13a, b, and 13c presents nonbreaking, breaking, and broken wave conditions at different water depths (air gap). The pressure sensor location was also normalized by water depth, h of each trial. Therefore, $z'/h = 1$ indicates the still water level.

In the case of nonbreaking waves (T11, T15, T19), the peak pressure values are found at still water level ($z'/h \sim 1$), as shown in Fig. 12. The shape of the pressure profile of the three trials is uniform, and the

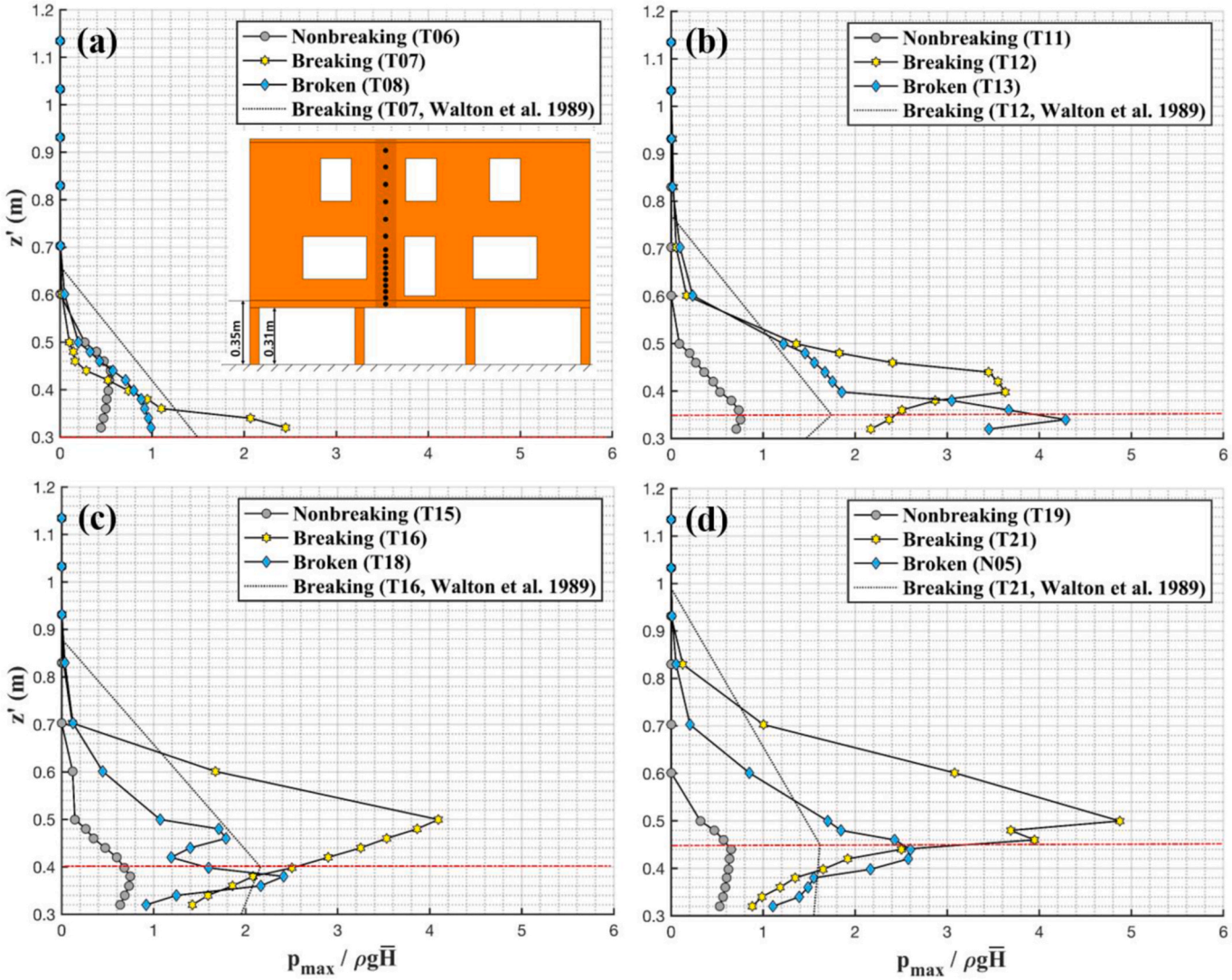

Fig. 12. Normalized pressure distributions for each water depth: (a) h = 0.30 m, (b) h = 0.35 m, (c) h = 0.40 m, and (d) h = 0.45 m. The horizontal dotted lines (red) in each plot represent water depth. Colors and marker types indicate nonbreaking (grey circle), breaking (yellow hexagram), and broken (sky diamond) waves. Pmax from Walton et al. (1989) provided dimensionless values (dotted line).

normalized peak pressure values are less than 0.8 (Fig. 13a). The cases of broken waves (T08, T13, T18) also have the peak pressure values near the still water level, but the shape of the profiles is not uniform (Fig. 13c). Especially, T13 showed an intense pressure on the lower part of the specimen, while T18 (Fig. 13c) showed much weaker and two different scaled peaks along the vertical line of the specimen. On the other hand, in the breaking waves (T12, T16, T21), the peak pressure values are found above the still water level ($z'/h = 1.1$–1.2) except T07 as wave slamming developed on the structure. The normalized peak pressure values ranged from 2.5 to 5.0, which are the largest among three different wave conditions except T12. In general, the largest wave loadings were observed at the breaking wave conditions, and the larger pressure was observed as the still water level increased. These patterns were also observed in previous experimental and numerical studies on elevated structures (Park et al., 2017; Park et al., 2018).

5.2. Vertical and horizontal forces on the elevated specimen

The maximum values of ensembled-averaged horizontal and vertical forces versus air gap (a) for all trials were shown in Fig. 14. For the horizontal forces, the adapted air gap (a') is applied as denoted in Section 2.2, while the default air gap (a) is applied for the vertical forces. The different marker types indicate nonbreaking (circle), breaking (star), broken (diamond) waves and varied colors indicate input wave heights at 0.1 m (green), 0.2 m (blue), 0.3 m (yellow), and 0.4 m (red). The effects of different air gaps versus vertical forces on the elevated structure are shown in Fig. 14a. The maximum forces are found at zero air gap ($a' = 0$) for H = 0.2, 0.3, 0.4 m and at $a' = -0.05$ for H = 0.1 m. Overall, the decreasing trend is found as the increase of the positive air gap. In contrast, the increasing trend is found as the decrease of air gaps to negative values. This dependency of vertical force on air gaps was also observed from the previous studies in Hayatdavoode et al. (2014), Seiffert et al. (2015), and Park et al. (2017). However, in Fig. 14b, the horizontal force shows an overall decreasing trend at the positive air gap conditions. Still, there is no clear correlation of the air gap to the horizontal force at the negative air gap conditions (submerged condition). Moreover, the peak horizontal forces at each air gap condition are found at different wave heights (0.1 m–0.4 m). Therefore, it is hard to find a simple correlation between the horizontal force and air gaps. Instead, we may consider both incident wave height and surge level (water depth) conditions with an air gap.

In the physical model studies of Duncan et al. (2021) presented a new parameter α, which is parameterizing both ensemble-averaged wave height and air gap to improve the equation for uplift pressure

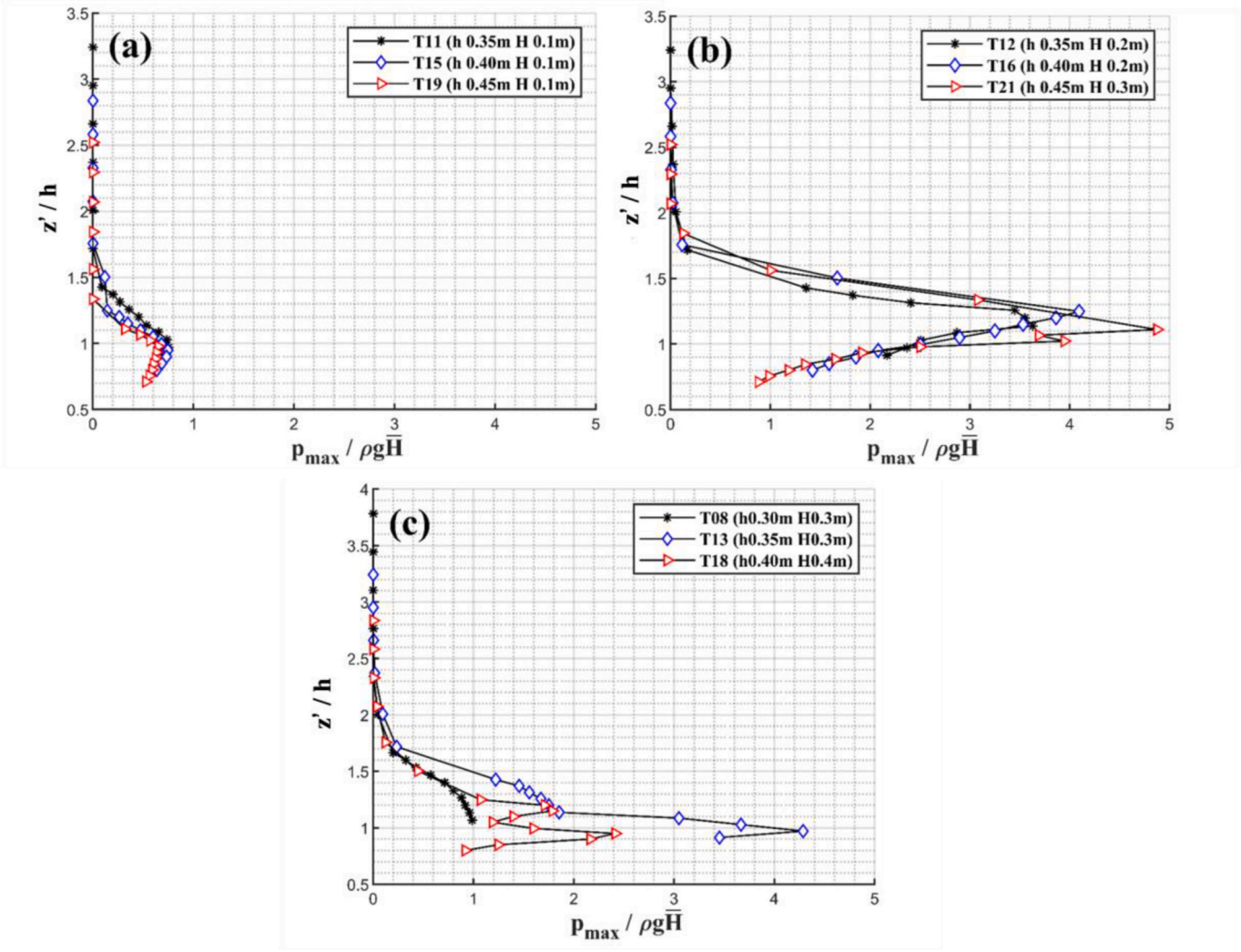

Fig. 13. Normalized pressure distribution for breaking wave conditions: (a) nonbreaking cases; T11 (black), T15 (blue), T19 (red), (b) breaking cases; T12 (black), T16 (blue), T21 (red), and (c) broken cases; T08 (black), T13 (blue), T18 (red).

distribution, which was:

$$\alpha = \overline{H} - a \tag{6}$$

In this study, to consider the horizontal forces acting in front of the specimen, the adapted air gap, a′ is used and normalized by water depth (surge level) h,

$$\frac{\alpha'}{h} = \frac{(\beta\overline{H} - a')}{h} \tag{7}$$

Here, $\overline{H}$ indicates the maximum value of the ensemble-averaged wave height near the specimen. Duncan et al. (2021) used the $\overline{H}$ at uswg4 for ensemble-averaged wave height to present vertical forces. However, we find that the use of uswg4 may overestimates the wave height to compare with other wave data due to the reflection from the specimen as it locates close to the specimen. Instead, we utilize the uswg7 or 5 to find the maximum wave height at each trial near the specimen (Fig. 1). We decide the higher wave height between uswg7 and 5 for Eq. (7). Therefore, the wave height at uswg7 is utilized for non-breaking wave cases, and uswg5 for breaking and broken wave cases. Those wave heights were already used in Fig. 13 to normalize the pressure at different wave breaking conditions. Furthermore, we introduce β, which is set as a unit value in our study for our shallow water condition, but it could be useful to adjust the new dimensionless parameter at different statistic wave formats and conditions (e.g., H_S, $H_{1/250}$ in random waves, solitary wave). We note that alternatively β could be specified less than unity to account for the fact that only the wave crest would be acting on the structure in many cases, such as the schematic example shown in Fig. 15. However, we consider $\overline{H}$ as the primary variable rather than the maximum water surface elevation because there may be cases where the air gap is negative (i.e., the structure is submerged below the still waterline). In this case, the total wave height (crest to trough) becomes more relevant. The conceptual sketch of Eq. (6) is provided in Fig. 15. It is noted here that the detailed configuration of girders is not clearly shown in this figure but found in detail in Fig. 2d.

To check a correlation between a new dimensionless parameter and horizontal forces on the elevated structure, we plot the dimensionless horizontal force versus α'/h in Fig. 16. The horizontal forces were normalized by the area of a frontal face of the superstructure (W × D) times the ensembled wave height ($\overline{H}$). Each W and D is the alongshore width and height of the superstructure of the specimen, which is equal to 1.83m and 0.87 m (Fig. 2a). The different marker types indicate non-breaking (circle), breaking (star), broken (diamond) waves, respectively, and surge level (flow depth) is varied from h = 0.2 m–0.45 m with different colors. Here, there is no horizontal force for all trial at h = 0.1 m. Compared with Fig. 14b, we can find a more apparent relationship between the nondimensionalized horizontal force and α'/h.

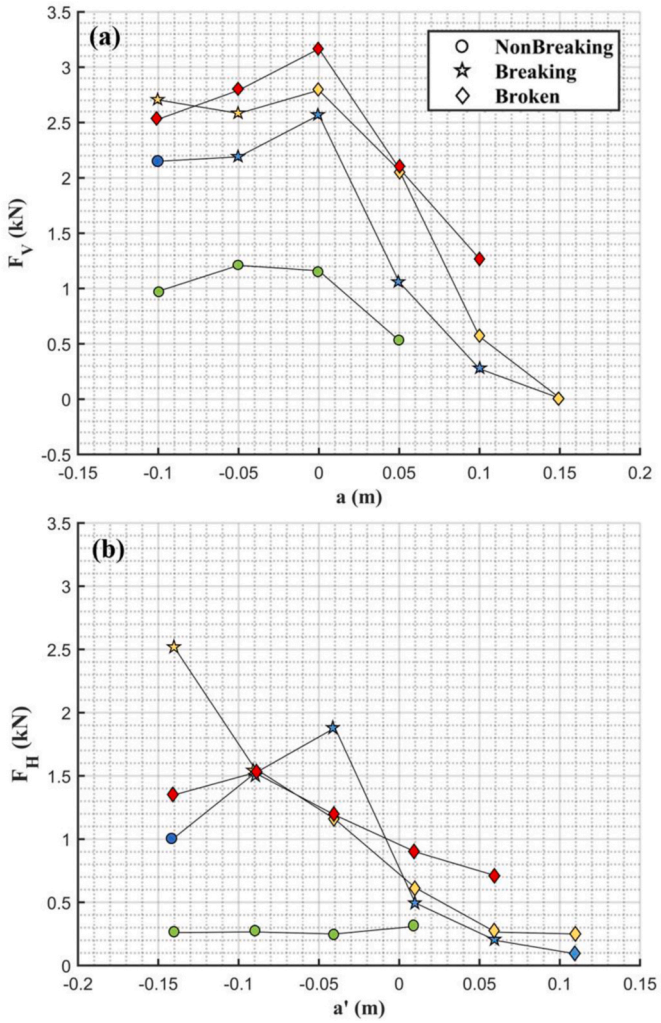

Fig. 14. (a) Vertical force vs. a ir gap and (b) horizontal force vs. adapted air gap for the trials with the same target wave height; $H = 0.1$ m (green), $H = 0.2$ m (blue), $H = 0.3$ m (yellow), and $H = 0.4$ m (red). Symbol types indicate nonbreaking (circle), breaking (star), and broken (diamond) wave conditions.

In addition to the experimental results in this study, the similar experimental results in the previous study (Park et al., 2017), which had measured horizontal and vertical forces on a simplified solid box-shaped (1.02 m × 1.02 m × 0.60 m) elevated structure, were utilized to validate and enhance the reliability of our new parameter to predict the horizontal forces. Fig. 17 shows both current numerical model results and previous experimental data from Park et al. (2017) with a fitted curve and 95% confidence intervals. Here, the fitted curve reveals the strong positive correlation between the new parameter (α'/h) and the horizontal force, and a new formula in the form of an power function is presented as:

$$\frac{F_H}{\rho g W D \overline{H}} = 0.32\left(\frac{\alpha'}{h}\right)^{1.5} \tag{8}$$

6. Conclusion and discussions

In this study, the Computational Fluid Dynamic (CFD) model studies of wave and structure interactions on the elevated residential buildings under variant air gaps and waves are performed using the OpenFOAM. The simulated model results are quantitatively compared with the measured data of the recent physical model studies, which estimated the detailed vertical wave pressure on the wood-framed elevated structure under varied waves and surge conditions (Duncan et al., 2021). The numerical model precisely reproduced the details of the specimen used in the physical model, including the exact size of window openings to evaluate the hydrodynamics in the vicinity of the structure.

The numerical model validation was performed according to the different regular wave conditions and water levels by considering the different breaker types such as nonbreaking, breaking, and broken wave conditions. From the numerical modeling results, the following conclusion can be drawn:

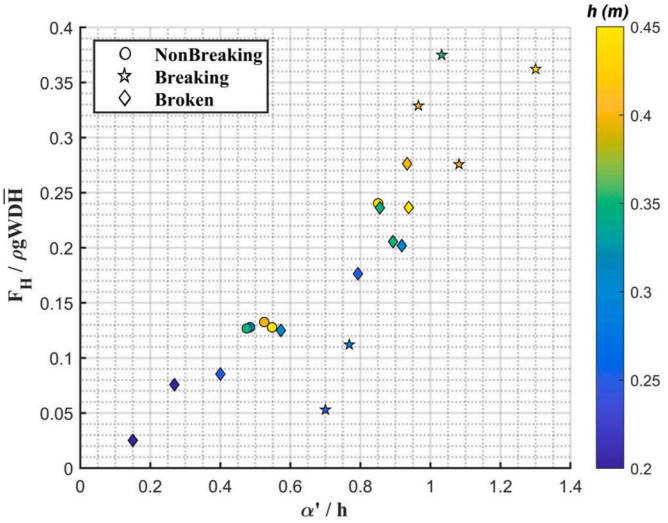

Fig. 16. Nondimensionalized horizontal force considering α'/h for different wave-breaking conditions. Different markers indicate nonbreaking (circle), breaking (star), and broken (diamond) waves. The color bar shows water depth.

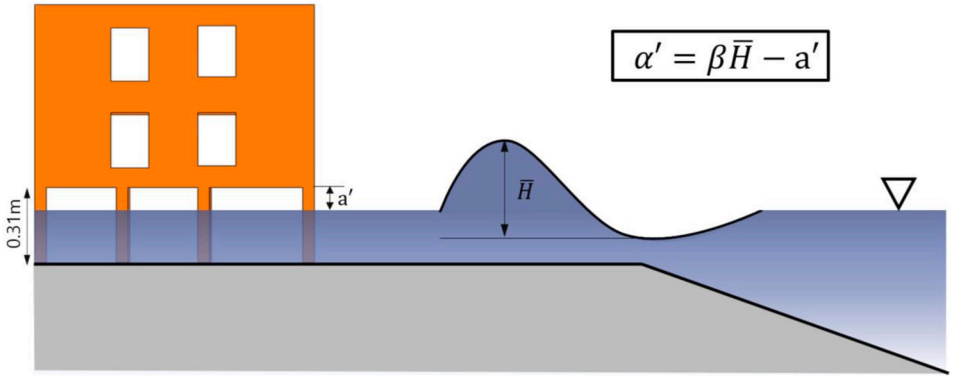

Fig. 15. Layout describing the definition of α' for horizontal forces.

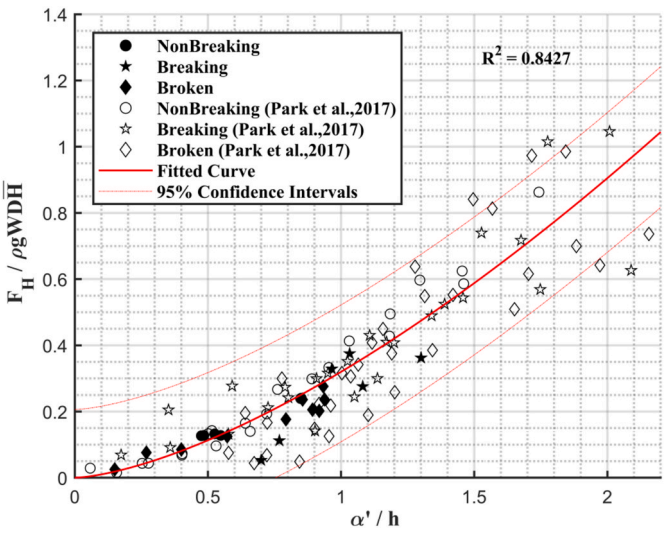

Fig. 17. Nondimensionalized horizontal force as a function of α'/h. The solid line presents the fitted curve (Eq. (8)) for this study and Park et al. (2017) and its 95% confidence interval (dashed line).

1. Overall, the numerical model successfully predicted the time evolution of surface water elevation, the horizontal fluid velocities at the front of the specimen, and the vertical pressure on the bottom of the elevated structure compared with the experimental results for all three-wave breaking conditions (nonbreaking, breaking, broken). The numerical results underestimate about 5.3% and overestimate 6.6% and 7.8% of the peak averaged vertical force to compare the experiment at the nonbreaking, breaking, and broken wave conditions, respectively.
2. The validated numerical model results reveal that the wave-induced horizontal pressure on the elevated structures shows different pressure distributions and scales depending on each wave breaking condition. Specifically, the normalized profile of the horizontal pressures shows quite a uniform profile at both nonbreaking and breaking wave conditions, while non-uniform profile at broken wave conditions. The maximum horizontal wave pressure is found near the still water level ($z'/h \sim 1.0$) for both nonbreaking and broken wave conditions, while above the still water level ($z'/h = 1.1$–1.2) for the breaking wave condition.
3. Both vertical and horizontal forces show different aspects to air gap conditions. The high correlation is found at the vertical force, while the low correlation is found at the horizontal force. The horizontal forces show a much more complicated pattern, and it is sensitive not only to the air gap but also to water depth and wave height conditions.
4. The new dimensionless parameter, α'/h, composing the incident wave height, air gap, and water depth, shows a high correlation to the horizontal forces.
5. A new empirical formula to predict a horizontal forces on the elevated structure showed that the normalized maximum horizontal force exponentially increased with the normalized α'/h, and the same pattern is found from the experimental data from the previous study (Park et al., 2017).

In this study, the numerical simulation was performed with the rigid structure assumption, while the actual physical experimental model allows the non-rigid motion, including vibrating and partial damages with loss of the structural components (e.g., external walls) as the input surge and wave conditions are getting severe from T01 to T21. The change of the opening conditions on the specimen will change the hydrodynamic conditions, especially in the inside of the structures. Moreover, the spatial distributions of the peak pressure at the front may not represent the whole spatial pressure fields because this study only utilizes the single vertical line at the frontal face to evaluate the pressure distributions. As a preliminary test, we compared the peak pressures to the spanwise direction and found major spatial pressure distribution due to 3D effects like windows and doors. Specifically, we evaluated T07 as a sample case, and we found that the average peak pressure among four observation points in a spanwise direction near the bottom line was 3412 Pa, while the standard deviation (STD) was 396 Pa. The exact pressure values and observation points are available in the appendix figure (Fig. A. 3). Even though this is a single trial, the deviation was not negligible, so we may aspect major spatial distribution of pressure at the wave impact depending on various opening conditions. Thus, it is recommended that additional studies evaluate detail hydrodynamic changes due to damaged conditions or various opening conditions on the buildings to quantify the 3-D effects on vertical and horizontal loadings at the elevated structures.

CRediT authorship contribution statement

Dayeon Lee: Methodology, Investigation, Conceptualization, Data curation, Formal analysis, Numerical Modeling, Writing – original draft, Writing – review & editing, Visualization. **Hyoungsu Park:** Methodology, Investigation, Conceptualization, Writing – review & editing, Supervision, Funding acquisition. **Taemin Ha:** Methodology, Investigation, Conceptualization, Numerical Modeling, Supervision. **Sungwon Shin:** Methodology, Investigation, Conceptualization, Data curation, Writing – review & editing, Supervision, Funding acquisition. **Daniel T. Cox:** Conceptualization, Writing – review & editing, Supervision, Funding acquisition.

Declaration of competing interest

The authors declare that they have no known competing financial interests or personal relationships that could have appeared to influence the work reported in this paper.

Acknowledgement

This material in this study is based upon work partially supported by National Research Foundation in Korea under awards 2022R1F1A1071641 and the National Science Foundation in the US under awards 1519679, 1661315 and 2203131. Any opinions, findings, and conclusions or recommendations expressed in this material are those of the author and do not necessarily reflect the views of the National Science Foundation.

Appendix

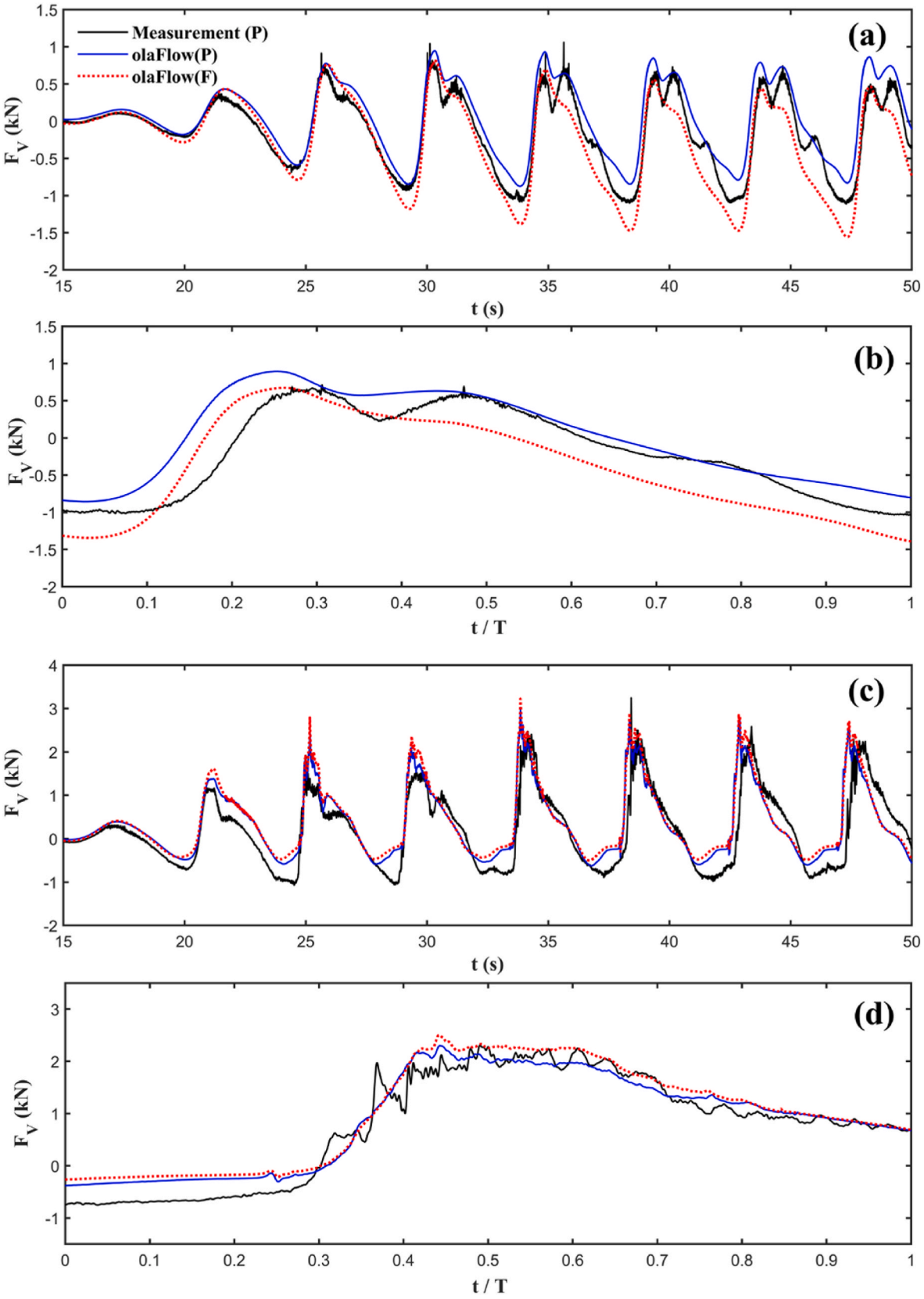

Fig. A.1. Comparisons of the vertical forces obtained by different three methods at T11(a-b, nonbreaking wave conditions) and T13(c-d, broken wave conditions). (a) and (c): The integration of the bottom pressure from the experiment (black solid line), the integration of the bottom pressure from the numerical model (blue solid line), and the acquisition directly in the numerical model (red dotted line) for T11 and T13 respectively. (b) and (d): Ensemble-averaged vertical forces for T11 and T13 respectively.

Table A.1
Ensemble averaged wave heights, horizontal force and vertical force from olaFlow.

Trial number	$\overline{H}$ (m) uswg5	$\overline{H}$ (m) Uswg7	F_H (N)	F_V (N)
T04	0.24	0.14	93	8
T05	0.21	0.16	250	11
N01	0.24	0.24	199	274
N02	0.20	0.16	264	565
N03	0.22	0.26	711	1 269
T06	0.13	0.16	310	530
T07	0.31	0.24	562	1 058
T08	0.32	0.18	616	2 361
N04	0.29	0.29	899	2085
T11	0.12	0.13	250	1 161
T12	0.30	0.32	1880	2 567
T13	0.36	0.27	1 157	2 792
T14	0.32	0.26	1 190	3 166
T15	0.13	0.12	266	1 209
T16	0.27	0.30	1 520	2 189
T17	0.36	0.34	1 560	2 582
T18	0.35	0.28	1 525	2 791
T19	0.13	0.11	261	976
T20	0.26	0.24	972	1 593
T21	0.41	0.45	2 516	2 704
N05	0.34	0.28	1 269	2 530

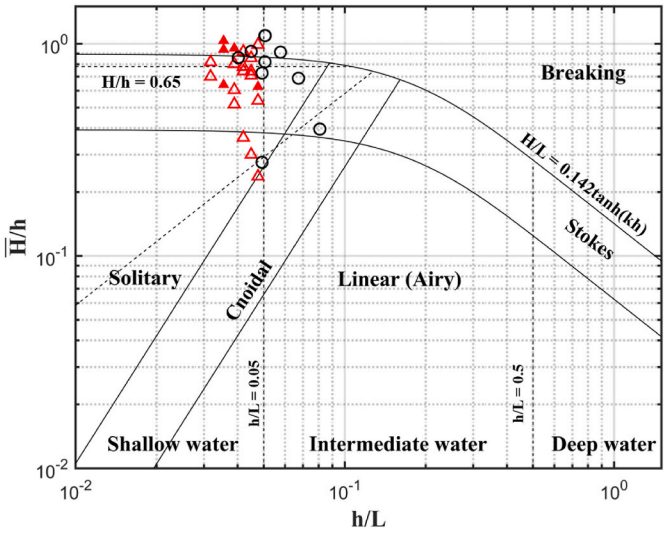

Fig. A.2. Wave classification (H/h vs. h/L) comparing this study at uswg 7 (red triangle) and Park et al. (2017) (black circle). Red triangle presents the experimental trials (hollow) and extra numerical trials(filled).

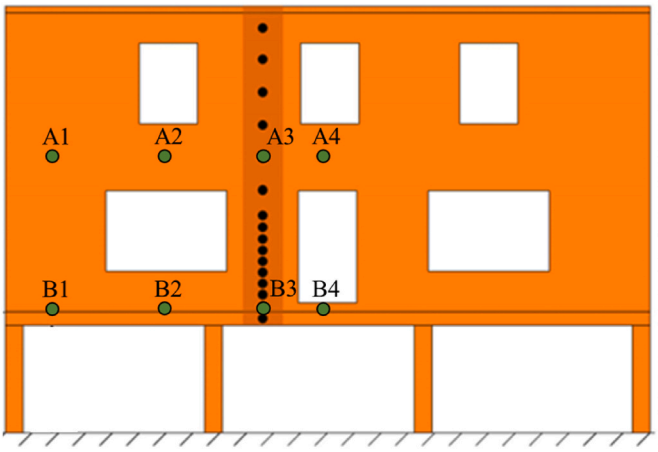

Row	1 (Pa)	2 (Pa)	3 (Pa)	4 (Pa)	Average /STD (pa)
A	16.4	21.4	13.9	14.6	16.6 /3.40
B	3648	3819	2945	3236	3412/396

Fig. A.3. Peak pressure variations in spanwise direction at the front (T07). The sketch of pressure observing points (upper panel) and peak value at each point (lower panel).

References

Bradner, C., Schumacher, T., Cox, D.T., Higgins, C., 2011. Large-scale laboratory measurements of wave forces on highway bridge superstructures. Proc. Coast. Eng. Conf. 3554–3566.

Bea, R.G., Xu, T., Stear, J., Ramos, R., 1999. Wave forces on decks of offshore platforms. J. Waterw. Port, Coast. Ocean Eng. 125 (3), 136–144.

Berberović, E., van Hinsberg, N., Jakirlić, S., Roisman, I., Tropea, C., 2009. Drop impact onto a liquid layer of finite thickness: dynamics of the cavity evolution. Phys. Rev. E 79 (3), 036306. https://doi.org/10.1103/PhysRevE.79.036306.

Burke, J., 2018. Structural Testing of a 1:6 Scaled, Light-Frame Construction, Near-Coastal, Residential Structure. M.S. Thesis, Oregon State University, Corvallis, USA.

Chen, X.B., Zhan, J.M., Chen, Q., Cox, D., 2016. Numerical modeling of wave forces on movable bridge decks. J. Bridge Eng. 21 (9), 04016055.

Cuomo, G., Tirindelli, M., Allsop, W., 2007. Wave-in-deck loads on exposed jetties. Coast. Eng. 54 (9), 657–679.

Cuomo, G., Shimosako, K., Takahashi, S., 2009. Wave-in-deck loads on coastal bridges and the role of the role of air. Coast. Eng. 56 (8), 793–809.

Cox, D., Barbosa, A., Alam, M., Park, H., Duncan, S., Lomonaco, P., 2021. Hydrodynamic tests on physical models of scaled wood frame shear-wall residential buildings. In: Progressive Damage and Failure of Wood-Frame Coastal Residential Structures Due to Hurricane Surge and Wave Forces. https://doi.org/10.17603/ds2-8evm-1y60. DesignSafe-CI.

del Jesus, M., Lara, J.L., Losada, I.J., 2012. Three-dimensional interaction of waves and porous coastal structures: Part I: numerical model formulation. Coast. Eng. 64, 57–72.

Desai, A., Jeffery, T., Moore, D., Turakhia, R., 2019. 2019 Storm Surge Report. CoreLogic, Irvine, CA.

Do, T.Q., van de Lindt, J.W., Cox, D.T., 2020. Hurricane surge-wave building fragility methodology for use in damage, loss, and resilience analysis. J. Struct. Eng. 146 (1), 04019177.

Duncan, S., Cox, D.T., Barbosa, A.R., Lomonaco, P., Park, H., Alam, M.S., Yu, C., 2021. Physical modeling of progressive damage and failure of wood-frame coastal residential structures due to waves and surge forces. Coast. Eng. 169 https://doi.org/10.1016/j.coastaleng.2021.103959.

Fema, P., 2011. Coastal Construction Manual: Principles and Practices of Planning, Siting, Designing, Constructing, and Maintaining Residential Buildings in Coastal Areas, 55.

Goda, Y., 1974. New wave pressure formulae for composite breakwaters. Copenhagen, Denmark. In: Proc. 14Th. *Asce Coastal Engng*. Conf., vol. 3, pp. 1702–1720. https://doi.org/10.9753/icce.v14.100. JUNE 24-28, 1974)).

Goda, Y., 2010. Random Seas and Design of Maritime Structures, third ed. World Scientific.

Hatzikyriakou, A., Lin, N., Gong, J., Xian, S., Hu, X., Kennedy, A., 2016. Component-based vulnerability analysis for residential structures subjected to storm surge impact from hurricane Sandy. Nat. Hazards Rev. 17 (1), 05015005 https://doi.org/10.1061/(ASCE)NH.1527-6996.0000205.

Huang, B., Zhu, B., Cui, S., Duan, L., Zhang, J., 2018. Experimental and numerical modelling of wave forces on coastal bridge superstructures with box girders, Part I: regular waves. Ocean Eng. 149, 53–77.

Hayatdavoodi, M., Seiffert, B., Ertekin, R.C., 2014. Experiments and computations of solitary-wave forces on a coastal-bridge deck. Part II: deck with girders. Coast. Eng. 88, 210–228.

Higuera, P., Lara, J.L., Losada, I.J., 2013a. Realistic wave generation and active absorption for Navier-Stokes models: application to OpenFOAM. Coast. Eng. 71, 102–118.

Higuera, P., Lara, J.L., Losada, I.J., 2013b. Simulating coastal engineering processes with OpenFOAM. Coast. Eng. 71, 119–134.

Higuera, P., Losada, I.J., Lara, J.L., 2015. Three-dimensional numerical wave generation with moving boundaries. Coast. Eng. 101, 35–47.

IPCC, 2021. Summary for policymakers. In: Zhai, P., Pirani, A., Connors, S.L., Péan, C., Berger, S., Caud, N., Chen, Y., Goldfarb, L., Gomis, M.I., Huang, M., Leitzell, K., Lonnoy, E., Matthews, J.B.R., Maycock, T.K., Waterfield, T., Yelekçi, O., Yu, R., Zhou, B. (Eds.), Climate Change 2021: the Physical Science Basis. Contribution of Working Group I to the Sixth Assessment Report of the Intergovernmental Panel on Climate Change [Masson-Delmotte, V. Cambridge University Press (in press).

Kaplan, P., Murray, J.J., Yu, W.C., 1995. Theoretical Analysis of Wave Impact Forces on Platform Deck Structures. Offshore Technology OMAE, pp. 189–198.

Karny, M., 2018. Hydrodynamic Testing on a 1:6 Scale, Wood Framed Near-Coast Residential Structure. M.S. Thesis, Oregon State University, Corvallis, USA.

Kennedy, A., Rogers, S., Sallenger, A., Gravois, U., Zachry, B., Dosa, M., Zarama, F., 2011. Building destruction from waves and surge on the bolivar peninsula during hurricane Ike. J. Waterw. Port, Coast. Ocean Eng. 137 (132), 132–141. https://doi.org/10.1061/(ASCE)WW.

Lackey, M., 2011. Billion-dollar Weather and Climate Disasters. http://www.ncdc.noaa.gov/img/reports/billion/disasters2010.pdfi. (Accessed 6 March 2014).

Liu, S., Ong, M.C., Obhrai, C., Gatin, I., Vukčević, V., 2020. Influences of free surface jump conditions and different k− ω SST turbulence models on breaking wave modelling. Ocean Eng. 217, 107746.

Maza, M., Lara, J.L., Losada, I.J., 2015. Tsunami wave interaction with mangrove forests: a 3-D numerical approach. Coast. Eng. 98, 33–54. https://doi.org/10.1016/j.coastaleng.2015.01.002.

Mendelsohn, R., Emanuel, K., Chonabayashi, S., 2012. The impact of climate change on global tropical cyclone damage. Nat. Clim. Change 2, 205–209. https://doi.org/10.1038/nclimate1357.

Menter R., F., 1993. Zonal Two Equation k-ω Turbulence Models for Aerodynamic Flows. Am. Inst. Aeronaut. Astronaut. https://doi.org/10.2514/6.1993-2908.

OpenCFD, 2017. OpenFOAM – the Open Source CFD Toolbox – User Guide. OpenCFD Limited.

Park, H., Do, T., Tomiczek, T., Cox T., D., van de Lindt W., J., 2018. Numerical modeling of non-breaking, impulsive breaking, and broken wave interaction with elevated coastal structures: Laboratory validation and inter-model comparisons. Ocean Eng. 158, 78–98. https://doi.org/10.1016/j.oceaneng.2018.03.088.

Park, H., Tomiczek, T., Cox, D.T., van de Lindt, J.W., Lomonaco, P., 2017. Experimental modeling of horizontal and vertical wave forces on an elevated coastal structure. Coast. Eng. 128 (January), 58–74. https://doi.org/10.1016/j.coastaleng.2017.08.001.

Pistrika, A., Jonkman, S.N., 2010. Damage to residential buildings due to flooding of New Orleans after hurricane Katrina. Nat. Hazards 54, 413–434. https://doi.org/10.1007/s11069-009-9476-y.

Qi, Z.X., Eames, I., Johnson, E.R., 2014. Force acting on a square cylinder fixed in a free-surface channel flow. J. Fluid Mech. 756, 716–727.
Rusche, H., 2002. Computational Fluid Dynamics of Dispersed Two-phase Flows at High Phase Fractions. Ph.D. thesis. Department of Mechanical Engineering, Imperial College of Science, Technology & Medicine, London. School of Civil Engineering, University of Cantabria, Cantabria, Spain, 2015.
Różyński, G., Hung, N., Ostrowskio, R., 2009. Climate change related rise of extreme typhoon power and duration over south-east asia seas. Coast. Eng. 51 (3), 205–222. https://doi.org/10.1142/S0578563409002028.
Seiffert, B.R., Hayatdavoodi, M., Ertekin, R.C., 2015. Experiments and calculations of cnoidal wave loads on a coastal-bridge deck with girders. Eur. J. Mech. B Fluid 52, 191–205.
Small, C., Blanpied, T., Kauffman, A., O'Neil, C., Proulx, N., Rajacich, M., Simpson, H., White, J., Spaulding, M.L., Baxter, C.D., Swanson, J.C., 2016. Assessment of damage and adaptation strategies for structures and infrastructure from storm surge and sea-level rise for a coastal community in Rhode Island, United States. J. Mar. Sci. Eng. 4 (4), 67.
Tomiczek, T., Kennedy, A., Rogers, S., 2013. Collapse limit state fragilities of wood-framed residences from storm surge and waves during hurricane Ike. J. Waterw. Port, Coast. Ocean Eng. 140 (1), 43–55. https://doi.org/10.1061/(asce)ww.1943-5460.0000212.
Tomiczek, T., Wyman, A., Park, H., Cox, D.T., 2019. Modified Goda equations to predict pressure distribution and horizontal forces for design of elevated coastal structures. J. Waterw. Port, Coast. Ocean Eng. 145 (6), 1–16. https://doi.org/10.1061/(ASCE)WW.1943-5460.0000527.
van de Lindt, J.W., Gupta, R., Garcia, R.A., Wilson, J., 2009. Tsunami bore forces on a compliant residential building model. Eng. Struct. 31 (11), 2534–2539. https://doi.org/10.1016/j.engstruct.2009.05.017.
Walton Jr., T.L., Aherns, J.P., Truitt, C.L., Dean, R.G., 1989. Criteria for Evaluating Coastal Flood-Protection Structures. COASTAL ENGINEERING RESEARCH CENTER VICKSBURG MS.
Wiebe, D.M., Park, H., Cox, D.T., 2014. Application of the Goda pressure formulae for horizontal wave loads on elevated structures. KSCE J. Civ. Eng. 18 (6), 1573–1579. https://doi.org/10.1007/s12205-014-0175-1.
Wilson, J.S., 2008. Behavior of a 1/6th Scale, Two-Story, Wood Framed Residential Structure under SurgeWave Loading. Oregon State University.
Wilson, J.S., Gupta, R., van de Lindt, J.W., Clauson, M., Garcia, R., 2009. Behavior of a one-sixth scale wood-framed residential structure under wave loading. J. Perform. Constr. Facil. 23 (5).
Wu, S., 2016. Effect of Skew on Seismic Performance of Bridges with Seat-type Abutments. University of Nevada. ProQuest Dissertations Publishing, Reno, 10252386.
Xian, S., Lin, N., Hatzikyriakou, A., 2015. Storm surge damage to residential areas: a quantitative analysis for Hurricane Sandy in comparison with FEMA flood map. Nat. Hazards 79 (3), 1867–1888. https://doi.org/10.1007/s11069-015-1937-x.